

AD-A161 181

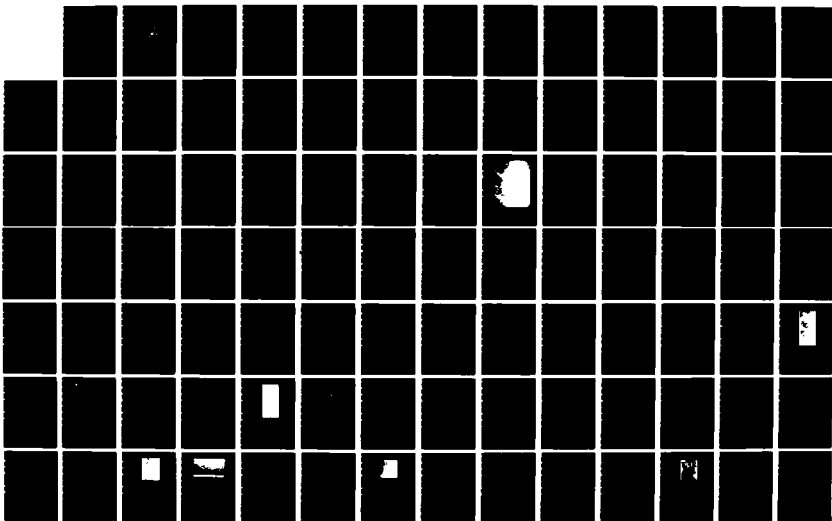
DETECTION OF SHOALS IN SEASAT SYNTHETIC APERTURE RADAR
IMAGERY: SELECTED CASE STUDIES(U) NAVAL POSTGRADUATE
SCHOOL MONTEREY CA R L DICKERMAN SEP 85

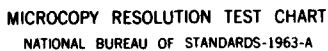
1/2

UNCLASSIFIED

F/G 8/10

NL





MICROCOPY RESOLUTION TEST CHART
NATIONAL BUREAU OF STANDARDS-1963-A

AD-A161 181

NAVAL POSTGRADUATE SCHOOL
Monterey, California



DTIC
ELECTE
NOV 19 1985
S A D

THESIS

DETECTION OF SHOALS
IN SEASAT SYNTHETIC APERTURE RADAR IMAGERY:
SELECTED CASE STUDIES

by

Ronald L. Dickerman

September 1985

Thesis Advisor:

James L. Mueller

Approved for public release; distribution unlimited

DTIC FILE COPY

11 19-85 044

Unclassified

SECURITY CLASSIFICATION OF THIS PAGE (When Data Entered)

REPORT DOCUMENTATION PAGE		READ INSTRUCTIONS BEFORE COMPLETING FORM
1. REPORT NUMBER	2. GOVT ACCESSION NO. AD-A161 181	3. RECIPIENT'S CATALOG NUMBER
4. TITLE (and Subtitle) Detection of Shoals in SEASAT Synthetic Aperture Radar Imagery: Selected Case Studies		5. TYPE OF REPORT & PERIOD COVERED Master's Thesis September 1985
		6. PERFORMING ORG. REPORT NUMBER
7. AUTHOR(s) Ronald L. Dickerman		8. CONTRACT OR GRANT NUMBER(s)
9. PERFORMING ORGANIZATION NAME AND ADDRESS Naval Postgraduate School Monterey, California 93940		10. PROGRAM ELEMENT, PROJECT, TASK AREA & WORK UNIT NUMBERS
11. CONTROLLING OFFICE NAME AND ADDRESS Naval Postgraduate School Monterey, California 93940		12. REPORT DATE September 1985
		13. NUMBER OF PAGES 141
14. MONITORING AGENCY NAME & ADDRESS (if different from Controlling Office)		15. SECURITY CLASS. (of this report) UNCLASSIFIED
		15a. DECLASSIFICATION/DOWNGRADING SCHEDULE
16. DISTRIBUTION STATEMENT (of this Report) Approved for public release; distribution unlimited		
17. DISTRIBUTION STATEMENT (of the abstract entered in Block 20, if different from Report)		
18. SUPPLEMENTARY NOTES		
19. KEY WORDS (Continue on reverse side if necessary and identify by block number) Satellite bathymetry, SEASAT, Synthetic aperture radar, Remote sensing, Bathymetric chart revision, Hydrographic survey planning, Radar, Shelikof Strait.		
20. ABSTRACT (Continue on reverse side if necessary and identify by block number) Ocean-going vessels have increased in size and draft in recent years, making traditional waterways too shallow and dangerous for use, and new shipping methods and increased costs require shorter transit times. Therefore, as new shipping routes are being sought, limited hydrographic survey resources must be efficiently applied. This study sought to demonstrate the feasibility of synthetic aperture radar (SAR) imagery as a tool for hydrographic presurvey planning by analyzing SAR imagery of Shelikof Strait, Alaska.		

DD FORM 1 JAN 73 1473

EDITION OF 1 NOV 65 IS OBSOLETE
S/N 0102-LF-014-6601

1

Unclassified

SECURITY CLASSIFICATION OF THIS PAGE (When Data Entered)

Unclassified

SECURITY CLASSIFICATION OF THIS PAGE (When Data Entered)

Anomalous brightness patterns visible in SAR imagery were related to interactions between ocean phenomena and bathymetric features, and an analysis of wave refraction was performed using optical Fourier transform (OFT)-measured wave spectra. The study results showed surface gravity wave refraction as measured by OFT's can be used to make quantitative estimates of water depths, generally within 40% error. Also, anomalous brightness patterns visible in SAR imagery indicate possible hazards to navigation. However, the absence of an anomalous pattern does not mean a hazard is not present.

Accession For	
NTIS CRA&I	<input checked="checked" type="checkbox"/>
DTIC TAB	<input type="checkbox"/>
Unannounced	<input type="checkbox"/>
Justification	
By	
Distribution/	
Availability Codes	
Dist	Avail and/or Special
A1	



16-48700-1 (Rev. 11-66)

Unclassified

Approved for public release; distribution unlimited

Detection of Shoals in SEASAT Synthetic Aperture Radar
Imagery:
Selected Case Studies

by

Ronald L. Dickerman
B.A. University of Connecticut, 1978

Submitted in partial fulfillment of the
requirements for the degree of

MASTER OF SCIENCE IN OCEANOGRAPHY (HYDROGRAPHY)

from the

NAVAL POSTGRADUATE SCHOOL
September 1985

Author:

R. L. Dickerman

Ronald L. Dickerman

Approved By:

James L. Mueller
James L. Mueller, Thesis Advisor

Stevens P. Tucker

Stevens P. Tucker, Reader

Christopher N. K. Mooers

Christopher N. K. Mooers, Chairman
Department of Oceanography

John N. Dyer
John N. Dyer, Dean of Science and Engineering

ABSTRACT

Ocean-going vessels have increased in size and draft in recent years, making traditional waterways too shallow and dangerous for use, and new shipping methods and increased costs require shorter transit times. Therefore, as new shipping routes are being sought, limited hydrographic survey resources must be efficiently applied. This study sought to demonstrate the feasibility of synthetic aperture radar (SAR) imagery as a tool for hydrographic presurvey planning by analyzing SAR imagery of Shelikof Strait, Alaska.

Anomalous brightness patterns visible in SAR imagery were related to interactions between ocean phenomena and bathymetric features, and an analysis of wave refraction was performed using optical Fourier transform (OFT)-measured wave spectra. The study results showed surface gravity wave refraction as measured by OFT's can be used to make quantitative estimates of water depths, generally within 40% error. Also, anomalous brightness patterns visible in SAR imagery indicate possible hazards to navigation. However, the absence of an anomalous pattern does not mean a hazard is not present.

TABLE OF CONTENTS

I.	INTRODUCTION.....	12
A.	OBJECTIVE.....	12
B.	BACKGROUND.....	12
C.	APPROACH.....	15
II.	SYNTHETIC APERTURE RADAR.....	19
A.	SAR IMAGING PRINCIPLES.....	19
B.	OCEANIC PHENOMENA.....	26
	1. Gravity Wave Refraction.....	27
	2. Non-Linear Gravity Wave Interaction Over Shoals.....	28
	3. Changes in Current Velocity.....	28
	4. Coastal Upwelling.....	36
	5. Internal Waves.....	38
	6. Fresh-water Runoff.....	39
III.	DATA AND METHODS.....	41
A.	TEST DATA.....	41
	1. Sar Imagery.....	41
	2. Control Data.....	41
	3. Oceanographic and Meteorological Data.....	43
B.	STUDY AREAS.....	45
C.	VISUAL INSPECTION OF FEATURES.....	47
	1. Internal Wave Signatures.....	47

2.	Shear.....	48
3.	Non-linear Gravity Wave Interaction.....	48
D.	OFT ANALYSIS OF SURFACE GRAVITY WAVES.....	50
1.	Wave Refraction.....	50
2.	Optical Fourier Transforms.....	53
E.	ASSESSMENT OF DATA QUALITY AND ERROR SOURCES....	55
IV.	ANALYSIS.....	59
A.	OVERVIEW OF THE PHYSICAL ENVIRONMENT.....	59
1.	Geographic Setting and Bathymetry.....	59
2.	Tides and Currents.....	60
3.	Density Stratification.....	64
4.	Wind Conditions.....	65
B.	CASE STUDIES OF LOCAL SUBAREAS.....	65
1.	Area I: Internal Waves and Surface Gravity Wave Refraction.....	66
2.	Area II: Internal Waves, Brightness Anomalies and Surface Gravity Wave Refraction.....	71
3.	Area III: Brightness Anomalies and Surface Gravity Wave Refraction.....	79
4.	Area IV: Brightness Anomalies and Surface Gravity Wave Refraction.....	80
5.	Area V: Brightness Anomalies and Surface Gravity Wave Refraction.....	83
6.	Area VI: Brightness Anomalies and Surface Gravity Wave Refraction.....	92

7. Area VII: Brightness Anomalies and Density Stratification.....	96
8. Area VIII: Surface Gravity Wave Refraction.....	100
C. SUMMARY.....	104
1. Internal Waves.....	105
2. Brightness Anomalies.....	106
3. OFT Analyses.....	108
V. DISCUSSION AND CONCLUSIONS.....	113
A. DISCUSSION.....	113
B. CONCLUSIONS.....	116
C. RECOMMENDATIONS.....	118
LIST OF REFERENCES.....	120
APPENDIX A: OPTICAL FOURIER TRANSFORMS.....	124
APPENDIX B: SURVEY HISTORIES.....	134
INITIAL DISTRIBUTION LIST.....	139

LIST OF TABLES

2.1	Seasat SAR System Characteristics.....	20
4.1	Wavelengths and Directions in Area I.....	71
4.2	Wavelengths and Directions in Area II.....	77
4.3	Wavelengths and Directions in Area III.....	80
4.4	Wavelengths and Directions in Area IV.....	81
4.5	Wavelengths and Directions in Area V.....	91
4.6	Wavelengths and Directions in Area VI.....	95
4.7	Wavelengths and Directions in Area VIII.....	100
4.8	Optical Fourier Transform Data.....	109
4.9	Optical Fourier Transform Prediction Accuracy.....	111
B.1	Hydrographic Survey Information For Afognak, NOS No. 5-4.....	136
B.2	Hydrographic Survey Information For Mt. Katmai, NOS No. 5-3.....	137
B.3	Hydrographic Survey Information For Iliamna, NOS No. 5-1.....	138

LIST OF FIGURES

1.1	Seasat coverage in Shelikof Strait, Alaska.....	16
2.1	Synthetic aperture radar footprint.....	22
2.2	Doppler range of radar return signals.....	24
2.3	A synthetic aperture radar and its parts.....	25
2.4	Signal intensity returned from a stationary surface.....	30
2.5	Signal Intensity returned from a surface with moving elements of constant velocity.....	31
2.6	Signal intensity returned from a surface with moving elements of varying velocity.....	32
2.7	SAR imagery of Nantucket Shoals - pseudo-imaging of bottom features.....	34
2.8	Schematic diagram of current, bathymetry and ultragravity wave interactions and the resultant SAR image intensity variation (Kasischke, et al, 1983).....	35
2.9	Comparison of SEASAT, LANDSAT and water depth data along a range line.....	37
3.1	Cotidal chart for M_2 tide component.....	44
3.2	Refraction of gravity waves incident upon a current.....	49
3.3	Refraction of gravity waves incident upon bathymetry.....	52
4.1	Principal bathymetric features in Shelikof Strait, Alaska.....	61
4.2	Imagery from Revolution 811 covering Area I.....	67
4.3	Bathymetry of Area I.....	69

4.4	Imagery from Revolution 811 covering Areas II, III and IV.....	72
4.5	Bathymetry of Area II.....	73
4.6	Bathymetry of Area III.....	74
4.7	Bathymetry of Area IV.....	82
4.8	Imagery from Revolution 811 covering Area V.....	84
4.9	Imagery from Revolution 289 covering Area V.....	85
4.10	Bathymetry of Area V, with transform locations D17, D16.....	86
4.11	Bathymetry of Area V, with transform locations G1, G2.....	87
4.12	Imagery from Revolution 323 covering Area V.....	88
4.13	Bathymetry of Area V, with transform locations F1, F2, F4.....	89
4.14	Imagery from Revolution 811 covering Area VI.....	93
4.15	Bathymetry of Area VI.....	94
4.16	Imagery from Revolution 323 covering Area VII.....	97
4.17	Bathymetry of Area VII.....	98
4.18	Water depths in Area VIII.....	101
4.19	Imagery from Revolution 811 covering Area VIII....	102
A.1	Optical Fourier Transform.....	125
A.2	OFT of evenly-spaced grating.....	126
A.3	OFT of evenly-spaced grating after rotation.....	126
A.4	Optical bench setup.....	127
A.5	k-Space wavelength.....	129
A.6	Transform wave heading.....	129
B.1	Index to bathymetric maps.....	135
B.2	Survey history for Afognak, NOS No. 5-4.....	136

B.3	Survey history for Mt. Katmai, NOS No. 5-3.....	137
B.4	Survey history for Iliamna, NOS No. 5-1.....	138

I. INTRODUCTION

A. OBJECTIVE

This thesis is an investigation of synthetic aperture radar (SAR) imagery as a tool for hydrographic surveying. The objective is to relate radar backscatter from surface wave phenomena to bathymetry and ocean bottom features. A descriptive interpretation of macro-scale features, (including internal wave signatures which are visible to the eye), and pseudo-imaging of shoals, is analyzed. Also, the Optical Fourier Transforms (OFT's) are used to estimate surface gravity wave refraction from SAR images of selected areas in Shelikof Strait, Alaska; linear wave refraction estimates are then used, in turn, to estimate water depths in shoaling areas.

B. BACKGROUND

Traditional waterways were established for ships with drafts of 35 feet and less, and are inadequate for modern containerized shipping methods and tankers (Goldsteen, 1982). Therefore, new shipping lanes must be found to allow the new, deeper-draft vessels to navigate waters which were previously unused. However, conventional hydrographic resources are inadequate to provide the accurate nautical

charts now required by both civilian and military users of these newer, larger ships (Hammack, 1977).

Only 16 percent of the world's oceans has adequate survey data to accurately represent the ocean bottom topography, and the time required to survey the remaining 84 percent using conventional survey methods is enormous. For example, a British study concluded that 284 ship years of work would be required to adequately survey Great Britain's territorial waters. (Hammack, 1977)

There are also severe financial constraints associated with acquiring detailed survey data. A well-equipped coastal survey vessel costs approximately \$20 million and has yearly operating expenses of \$1.4-3.0 million (Goodfellow, 1982). The cost of an average survey approaches \$3500 per square mile (Collins, 1978). The Shelikof Strait areas examined in this study cover approximately 7,000 square miles. Thus, it would cost \$24.5 million to adequately survey this area.

Because survey resources are limited (Hammack, 1977), a remote sensing instrument, such as SAR, could be used as a planning tool for directing the application of those resources at a minimal cost. The imagery used in this study cost \$2,500 for processing; and the cost of collecting the raw data should be negligible once the satellite is in orbit.

A synthetic aperture radar measures a signal backscattered by the Bragg scattering cross section of 30 cm ultragravity waves on the ocean surface. Bathymetric features have been shown to influence this cross section indirectly, with the effect of revealing the shapes of shoals in distinct patterns of brightness modulation in the SAR image (Plant, et al., 1978, Evans and Shemdin, 1980, Alpers, et al., 1981, Brown, et al., 1976, McLeish, et al., 1980 and Kasischke, et al., 1983). Perhaps the most dramatic example is the almost one-to-one relationship between the SAR-imaged ultragravity waves and the bottom sand waves in Nantucket Shoals (Kasischke, et al., 1980 and Valenzuela, et al., 1983). This example will be reviewed in Chapter II of this thesis.

Other examples of oceanic processes that have distinct SAR signatures are: (1) wave refraction, (Shuchman, et al., 1979), (2) non-linear gravity wave interaction, (Kasischke, et al., 1980, (3) upwelling, (Kasischke, et al., 1982), and (4) internal wave manifestations (Shuchman and Kasischke, 1979). Wave refraction occurs as a surface gravity wave propagates shoreward over a shoaling bottom; both the wave direction and wavelength change as a linear function of water depth. If a surface gravity wave encounters an abrupt change in depth, such as a coral reef or submerged rock, the ensuing wave transition strains the ultragravity wave field. Colder, deep water rising to the surface (upwelling)

modulates the ultragravity wave structure in two ways: 1) the convergence of temperature and biological influences vary surface tension as a restoring force, and 2) the planetary boundary layer is more stable over colder water than over warmer water, and hence, wind stress is lower, showing up as darker areas in SAR imagery. When a current flows over a topographic bottom feature, internal waves can be generated which modulate the surface ultragravity wave field.

The evidence is clear that SAR signatures indicate the presence of various bottom configurations, and that SAR can be used to locate at least some areas of potential danger to ocean and coastal navigation. SAR signatures of bathymetric phenomena may be catalogued for use by an image analyst, and wave refraction estimation techniques may be used to estimate depths from SAR imagery. A hydrographic survey planner can use this type of information to optimize allocation of survey resources, scheduling high priority areas where possible hazards are indicated for immediate surveying, and leaving other areas for surveying at a later date.

C. APPROACH

Shelikof Strait, Alaska is typical of areas of consideration for new shipping routes, and extensive resources would be required to adequately survey the area.

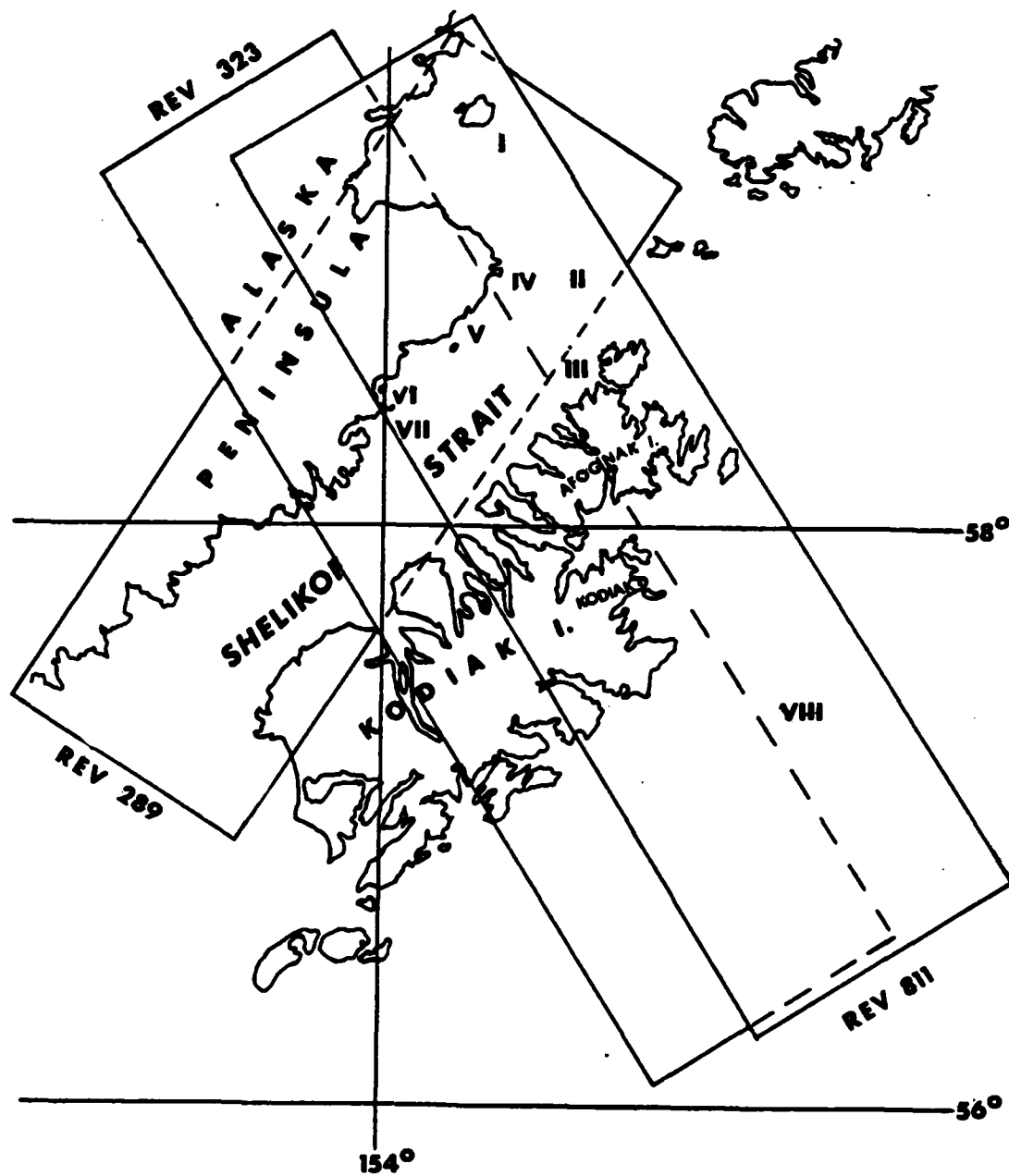


Figure 1.1. SEASAT Coverage in Shelikof Strait, Alaska.

Therefore, SAR images were obtained for analysis and bathymetric maps of Shelikof Strait were obtained to use as a reference for the analysis.

The SAR images and subareas were first examined to identify obvious anomalies or patterns in the radar cross section modulation which might be associated with bathymetry. These signatures were then compared to colocated bathymetric features as shown on bathymetric maps of the area. The bathymetric maps were also reviewed to identify areas where gravity wave refraction was likely to occur. In those selected areas, Optical Fourier Transforms (OFT) were acquired and analyzed to infer surface gravity wave refraction (change in wavelength and direction) for comparison with changes predicted using linear wave refraction and charted water depths.

Shelikof Strait was chosen as the study area due to the availability of both bathymetric maps based on recent surveys and SAR imagery from three SEASAT orbits (Fig. 1.1). Also, this area is representative of the types of waterways which are candidates for new shipping routes. The disadvantage to studying Shelikof Strait is that it is sheltered from the deep ocean swell; this limited the wavelength and amplitude of gravity waves available to illuminate shoaling features. However, because it is representative of likely candidates for deep-water shipping routes, it is a practical area to demonstrate the

feasibility of use of SAR to locate possible hazards to navigation in hydrographic presurvey planning.

II. SYNTHETIC APERTURE RADAR IMAGERY

A. SAR IMAGING PRINCIPLES

A SAR transmits a coherent electromagnetic pulse which is reflected back to the satellite by resonant (Bragg) scattering at the ocean surface. The Bragg scattering cross section, and therefore the strength of the returned pulse, depends directly on the spectral energy density (per unit area) of ocean surface waves of the Bragg wavelength

$$L_B = \lambda_r / 2 \sin \theta$$

where λ_r is the radar's electromagnetic wavelength and θ is the incidence angle measured from the normal to the sea surface. Stated simply, as the amplitudes of ocean waves of the Bragg wavelength grow larger, the strength of the reflected radar pulse increases, and vice versa.

The SAR emitted a 33.4 microsecond pulse at a wavelength of 23.5 cm at surface incidence angles spanning 19 to 25 degrees (Vesecky and Stewart, 1982). Other characteristics of this instrument are summarized in Table 2.1.

From the data in Table 2.1, it is apparent that ocean waves of length approximately 30 cm are responsible for Bragg scatter return measured by the SEASAT SAR. Ocean surface waves of this length are called "ultragravity

waves", which refers to a region of the spectrum where surface tension and gravity are of comparable importance as restoring forces. Variations in the amplitudes of 30 cm ultragravity waves may result from variations in wind stress, interactions with larger waves (a mechanism which helps visualize ocean swell in SAR images), surface stress variations associated with

Table 2.1. Seasat SAR System Characteristics
(Vesecky and Stewart, 1982)

Satellite altitude	800km
Imaged swath	100km
Angle of incidence	19°-25°
Resolution	25-40m
Radar wavelength	23.5cm
Contrast ratio	9db
Power, average	55W
Chirp pulse length	33.4 s
Bandwidth	19MHz
PRF	1463-1640Hz
Antenna	
Dimensions	10.7 x 2.16m
Gain	35db
Beam width	1.73° x 6.2°

convergence and divergence regions in surface flow, current wave interactions, and spatial variations in surface tension due to surfactants such as organic oil slicks (which are ubiquitous on the sea surface). Several of these mechanisms are, in turn, affected by variations in bottom topography, wave refraction, or both.

Cross track resolution is obtained by "range-gating" the return signal into successive time bins of length dt , which must be larger than the radar's transmitted pulse length. Referring to Figure 2.1, the cross-track range resolution in a single cell gated over time dt , is given by

$$dx = c \, dt / (2 \sin \theta)$$

where c is the speed of light and the other terms are defined in Figure 2.1. For the SEASAT SAR, a cross-track resolution of 25 m is associated with a range gate of approximately 62.4 ns; a pulse of this effective length was achieved by compressing the 33.4 μ s chirped pulse (Vesecky and Stewart, 1982).

A fine enough resolution to also resolve 25 m in the along-track direction is obtained, with a SAR, by synthesizing a very long radar aperture through Doppler processing. For an idealized monochromatic (a pure single frequency) radar, the only portion of the returning pulse which has the same frequency as the emitted pulse is that portion returning from the surface area perpendicular to the spacecraft's direction of travel. The portion of the pulse returning from the area forward of the 90° azimuth is Doppler-shifted to a higher frequency, and the return from the area behind 90° azimuth is Doppler-shifted to a lower frequency (Fig. 2.2). The Doppler change in frequency is

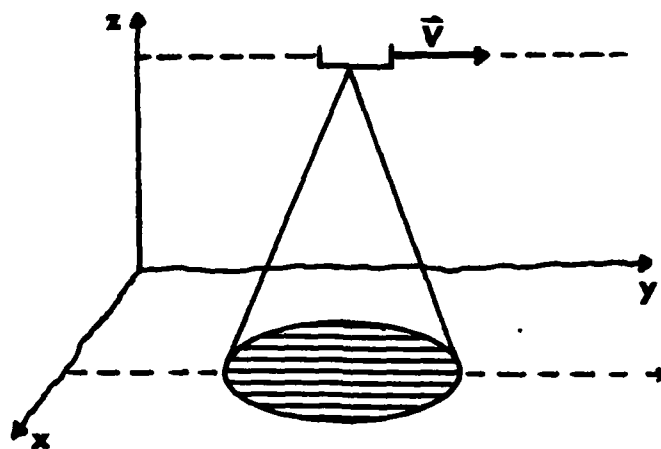
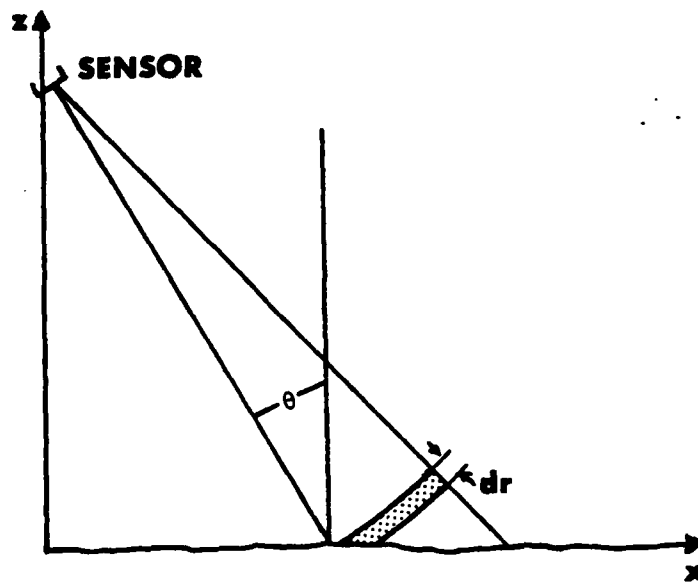


Figure 2.1. Synthetic Aperture Radar footprint.

nearly linear with small angles (in radians) measured from 90° . Therefore, discrete frequency and amplitude returns for each transmitted pulse can be assigned to a particular surface area. The information from a number of returns from a single surface area is then use to synthesize an image as if it were collected from a radar having a long aperture (Fig. 2.3).

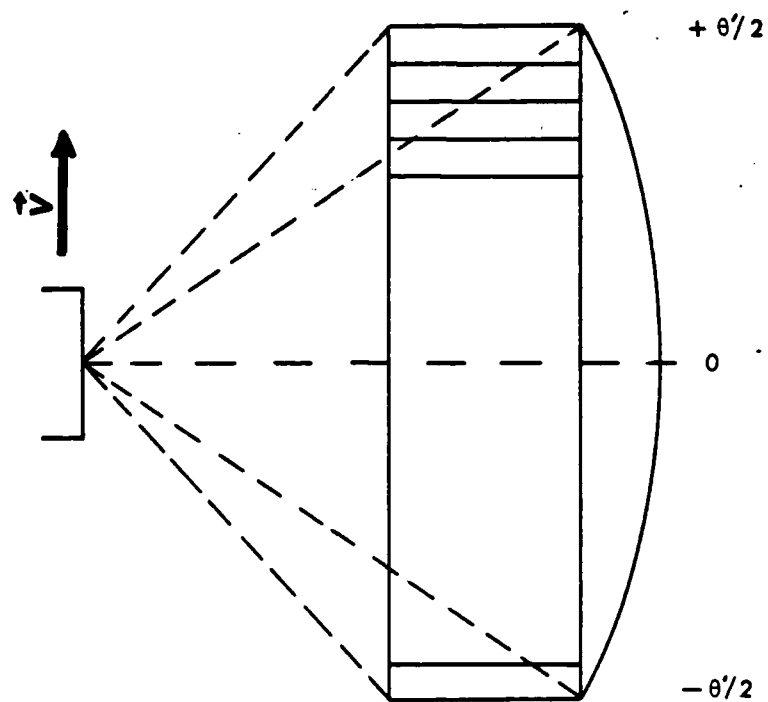
The along-track resolution for SEASAT is approximately,

$$dy = \lambda_r R / (2 L_s \cos \theta),$$

where R is the range (approx. 850km) and L_s is the length of the synthetic aperture (Vesecky and Stewart, 1982). For,

$$L_s = Vt = 17\text{km},$$

where V is satellite velocity (7.2km/s) and t is the sample length (2.3s), the along-track resolution is approximately 6.6m. However, SEASAT signal data was processed such that four resolution cells in the azimuth direction were incoherently averaged for a resulting resolution of 25m. The reader is referred to Alpers (1983), Tucker (1983) and Vesecky and Stewart (1982), for a more thorough discussion on the technical details of the SAR imaging process (including the extension of the Doppler processing concept, using phase coherence to sort the frequency spread of the



$$f = f_o + f_D$$

$$f_D = (2f_o v \sin \theta') / c \approx (2f_o v \theta') / c$$

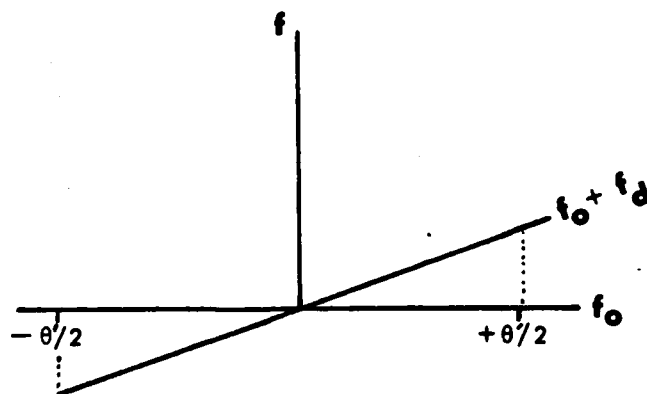


Figure 2.2. Doppler range of radar return signals.

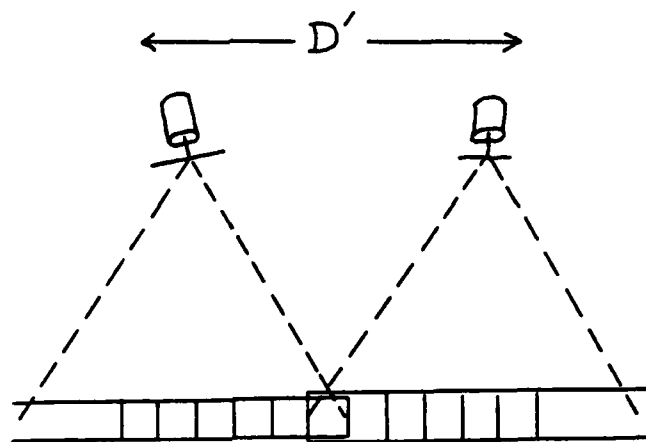


Figure 2.3. A Synthetic Aperture Radar and its parts.

transmitted radar pulse from that associated with Doppler shifts).

B. OCEANIC PHENOMENA

It has been empirically determined that L-band backscatter from the sea surface is proportional to $\underline{U}^{0.5 \pm 0.1}$, where \underline{U} is the surface wind velocity (Thompson, et al., 1983). If local winds are less than approximately 2 m/s (Kasischke, 1982), the surface will not have sufficient roughness to produce significant Bragg scattering; such areas will appear dark in SAR imagery. The reverse is also true. If the surface wind speed is greater than approximately 10 m/s, the number and magnitude of Bragg waves on the surface will saturate, resulting in a strong signal return devoid of distinct spatial features within the affected area.

There are a number of oceanic and atmospheric phenomena which affect the radar cross-section of Bragg waves. Some of these, (such as wind stress, currents, internal waves, wave diffraction and frontal boundaries) produce SAR image signatures without interacting with bottom topographic features (Kasischke, et al., 1982). In this study, we are concerned with discriminating phenomena which create distinctive SAR image signatures through interaction with bathymetry.

There are three categories of phenomena by which bottom topography may affect the amplitudes of Bragg waves and thus, the radar cross-section, seen as brightness modulations in a SAR image. These are refraction of ocean surface gravity waves propagating across shoaling bathymetry, interaction of surface waves with currents modulated by flow across bathymetric features (either directly seen by interaction of the the current shear with the Bragg waves or indirectly through generation of internal waves) and bathymetric forcing of flow which produces distinctive surface temperature patterns which affect the stability of the atmospheric planetary boundary layer.

1. Gravity Wave Refraction

A surface gravity wave propagating into shoaler water experiences wave refraction as a function of depth. If the changes in wavelength and direction can be measured, the depth can be calculated (see section III.D).

Optical Fourier Transforms of SAR images can be used to measure the changes in ocean wavelength and direction (Shuchman, et al., 1979a, McLeish, et al., 1980, Shuchman and Kasischke, 1981 and Meadows, et al., 1983). The wave direction derived from the SAR spectra will be shifted from the true wave direction as a function of the wave's direction relative to the SAR's viewing axis (Pawka, et al., 1980). However, for this study the change in relative wave directions is used to estimate the general orientation of

bottom features. Therefore, the direction bias due to wave motion should not affect the conclusions.

Ocean currents can also cause surface gravity wave refraction. Hayes (1980) showed the Gulf Stream refracted shoreward propagating waves enough so the change could be detected by SAR. Therefore, a certain amount of caution must be exercised when making estimates of depths from the magnitude of wave refraction.

2. Non-Linear Gravity Wave Interaction Over Shoals

Sharp changes in the image tone of SAR imagery have been related to shoal areas surrounded by deeper water (Kasischke, et al., 1980). Kasischke, et al., (1982) postulate that these brightness anomalies are associated with abrupt shoaling of the waters. It is surmised that the abrupt shoaling causes a rapid transition of gravity waves from deep water waves to shallow water waves, which in turn strains the ultragravity wave field and changes the radar backscatter returned to the sensor.

3. Changes in Current Velocity

Several SEASAT SAR images appear to contain direct images of bottom topography features (Kasischke, et al., 1983, Valenzuela, et al., 1983). However, electromagnetic waves of the length generated by the SEASAT SAR, 23.5cm, will only penetrate a few centimeters into the sea surface. Therefore, SAR must be imaging the results of an interaction between the bottom topography and an oceanic process

manifested on the ultragravity wave field on the ocean surface.

Conventional radar assumes either the sensor itself or the observed object is stationary. If a water surface element of high radar cross-section is held stationary on the sea surface and observed by SAR as the satellite crosses overhead the Doppler shift in the returning signal phase is a function only of the azimuth angle. In this case, the Doppler shift can be properly taken into account during processing (Shuchman, et al., 1981, Vesecky and Stewart, 1982, and Tomiyasu, 1976). Thus, the return signal from a particular water surface element can be determined from its Doppler shift and corrected to its instantaneous location in the radar beam as shown in Figure 2.4.

If the entire surface were to move at a constant velocity during the time the radar beam was crossing, the Doppler shift would be modified shifting the placement of the return signal intensity as shown in Figure 2.5 (Vesecky and Stewart, 1982). Note that the surface velocity vector must have a component in the azimuth direction or the Doppler shift will not be altered.

If the surface element having increased roughness were to move at a faster rate than the adjacent elements (i.e., a jet), the return signal intensity would again be shifted (Fig. 2.6): we would now observe an energy peak and adjacent minimum, because the adjacent element is not

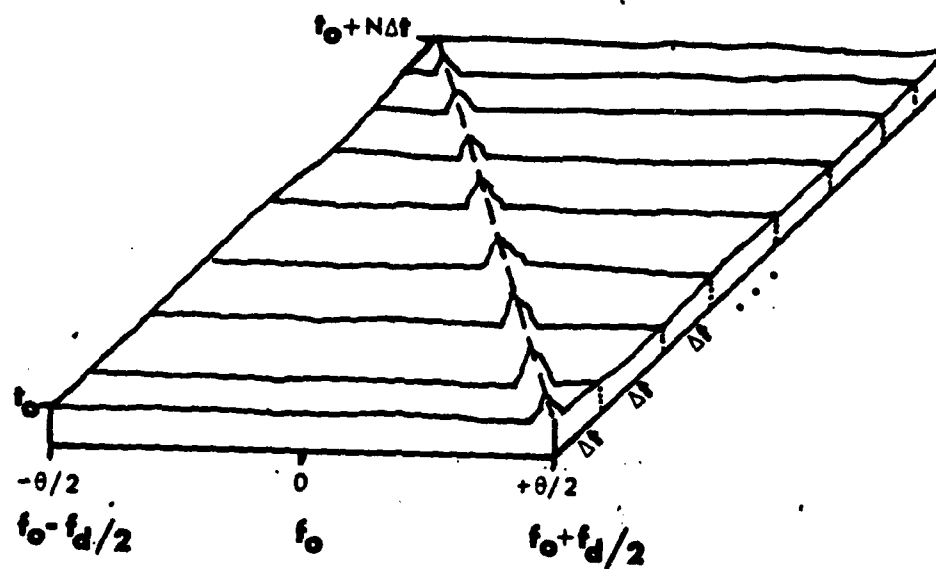


Figure 2.4. Signal intensity returned from a stationary surface.

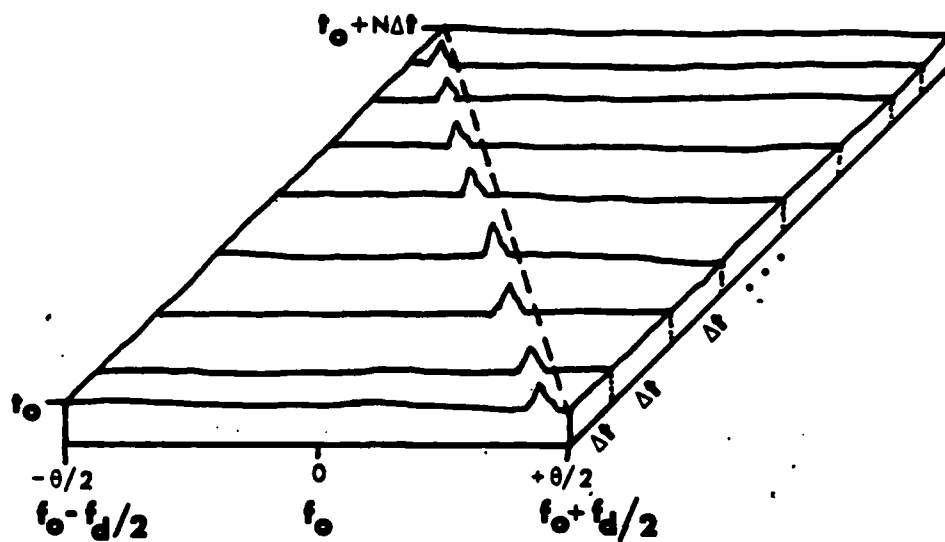


Figure 2.5. Signal intensity returned from a surface with moving elements of constant velocity.

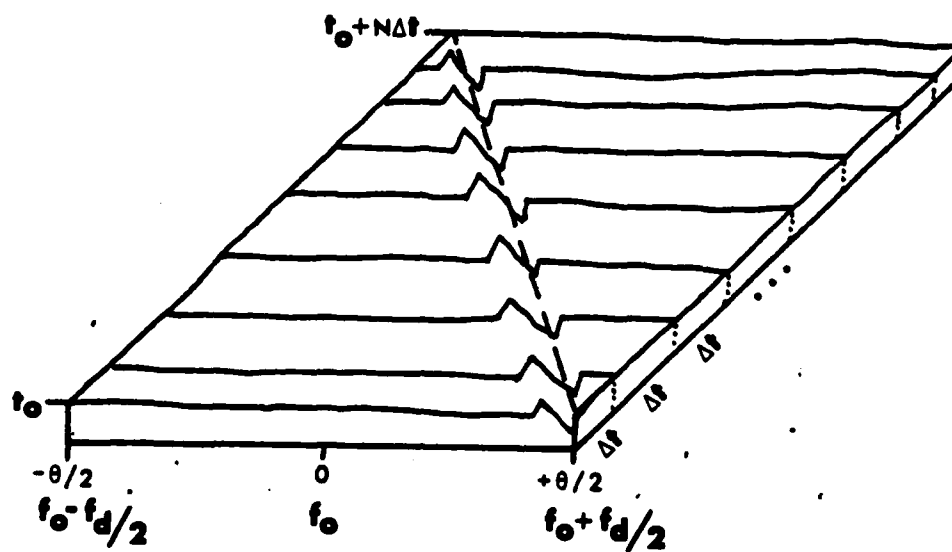


Figure 2.6. Signal intensity returned from a surface with moving elements of varying velocity.

filling in the 'space' for that particular Doppler return. As seen in SAR images, the energy peaks appear as brighter pixels and the minima appear as darker pixels.

In a SAR image of a region of strong surface current shear, velocity bunching tends to produce adjacent bright and dark bands across the edge of the shear zone. This effect, together with current-wave-bathymetry interactions produce SAR images of bathymetric relief.

Nantucket Shoals, where strong tidal currents flow across distinct shoals, has produced some of the more dramatic examples of this type of signature (Fig. 2.7). Environmental conditions required to observe this phenomenon at this site have been determined as: (1) a tidal current greater than 0.4 m/s, and (2) a wind velocity between 1 and 7.5 m/s (Kasischke, et al., 1983).

Figure 2.8 is a schematic illustration of the interactions between tidal currents, bottom topography and capillary waves, and is labelled to suggest the resulting variation in SAR image intensity. The dark tones of the SAR imagery correspond to areas where the current velocity increases due to a decrease in water depth, decreasing the amplitude of the ultragravity waves. The bright tones occur where increasing depth has slowed the current velocity, compressing the ultragravity waves (increasing their amplitude). The gray tones occur over areas of uniform depth, where the wind is able to restore the ultragravity



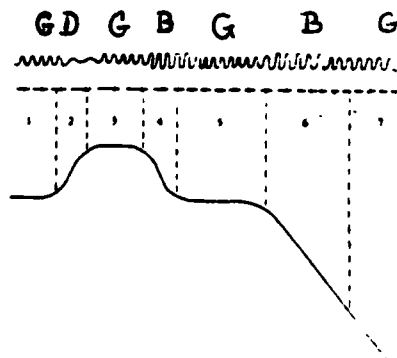
Figure 2.7. SAR imagery of Nantucket Shoals - pseudo-imaging of bottom features.

a.) FALLING TIDE

Radar Image Tone
Surface Roughness
Current Magnitude

Zone

Bottom

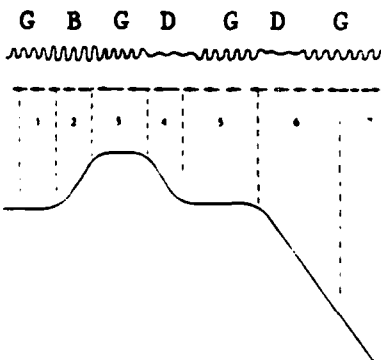


b.) RISING TIDE

Radar Image Tone
Surface Roughness
Current Magnitude

Zone

Bottom



B - Bright
D - Dark
G - Gray

Figure 2.8. Schematic diagram of current, bathymetry and ultra-gravity wave interactions and the resultant SAR image intensity variation (Kasischke, et al, 1983).

waves to equilibrium. The reader is referred to Kasischke, et al., (1983), for a more exacting description of this process.

Kasischke, et al., (1980) determined general correlations between this type of signature and the charted bathymetry for five areas: (1)DMA-Bahamas calibration area, (2) Southern Bahamas, (3) Nantucket Shoals, (4) English Channel, and (5) North Rona Rock. The correlation was done manually by placing a transparent reproduction of a chart over the SAR imagery. If there was a 50 percent change in water depth within a few hundred meters of a possible feature as shown on the SAR imagery, a correlation was assumed to exist; correlations for the five areas ranged between 60 and 100 percent.

Kasischke, et al., (1982) performed a more rigorous study of the relationship between SEASAT SAR imagery and water depths in Nantucket Shoals. They found a good correlation between signal intensity and water depth along single range lines, (Fig. 2.9). This result suggests that for well-defined situations, it may be possible to distinguish relative depth changes between discrete points.

4. Coastal Upwelling

In general, water in upwelling areas is colder, less saline (U.S. west coast, particularly) and richer in nutrients, all of which tend to decrease surface tension (Knauss, 1978). The decrease in surface tension, in turn,

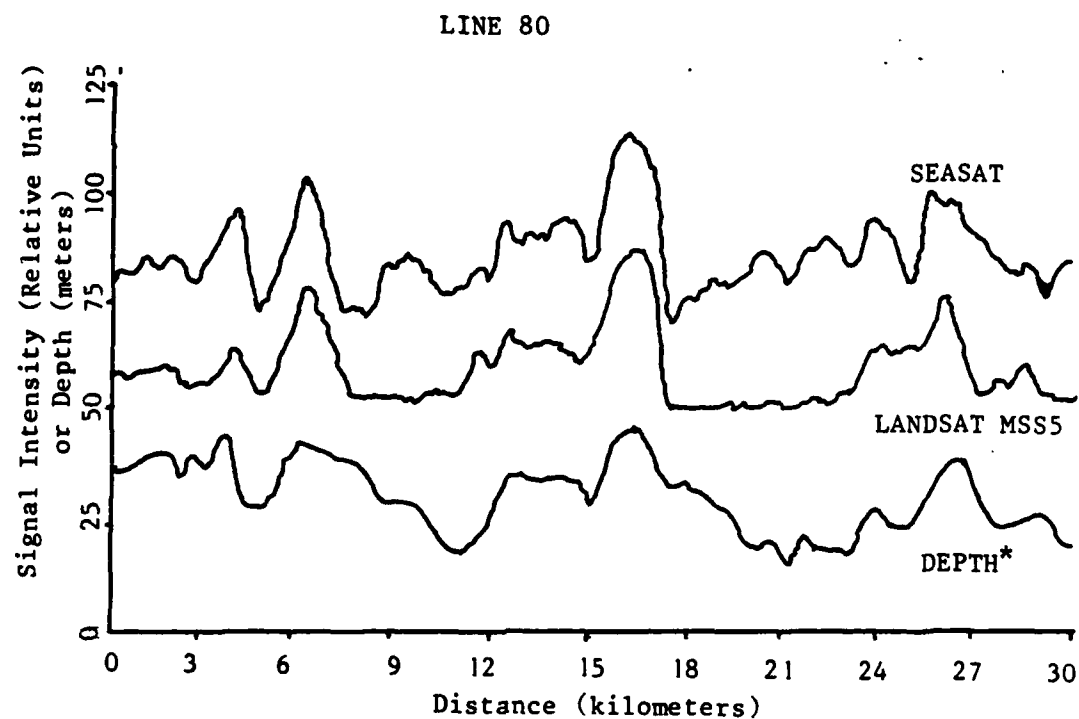


Figure 2.9. Comparison of SEASAT, LANDSAT and Depth data along a range line (Kasischke, et al, 1982).

*Depth value plotted as $50-Z$, where Z is depth in meters.

decreases the energy density of capillary and ultragravity waves on the surface, and therefore decreases the radar cross-section. Hence, ocean upwelling areas will have a dark appearance on SAR images.

Upwelling produces modulations in SAR images, both from surface dynamics associated with fronts, and due to changes in wind stress associated with the effect of changes in air-sea temperature differences (and thus, atmospheric planetary boundary layer stability), over cold upwelling regimes. Further, coastal upwelling is associated with topographic structure of the continental shelf and slope (Mooers, et al., 1977), and intense upwelling centers are often associated with submerged coastal headlands (Arthur, 1965) and over the heads of submarine canyons (Shaffer, 1976). Kasischke, et al. (1983) have related the appearance of a frontal boundary on a SAR image (revolution 762, August 19, 1978) to upwelling produced by current flow over a shelf in the Faeroe Islands Thompson and Golding (1981) showed that strong tidal suction around steep bottom slopes may induce upwelling. Hence, the appearance of an upwelling signature in SAR imagery may suggest the presence of a shallow bottom sloping steeply into deep water, or of a submerged headland (e.g. Arthur, 1965).

5. Internal Waves

The detection of internal waves by SAR has been well documented, (Trask and Briscoe, 1983, Alpers and Ettore,

1983, Hughes and Gower, 1983, Kasischke, et al., 1982, Shuchman and Kasischke, 1979, Beal, et al., 1981 and Allan, 1983). There are several processes which can generate internal waves, including wind stress, surface wave interaction, baroclinic instability, Ekman layer instability and current flow over a bottom feature. However they may be generated, internal waves create surface convergence/divergence zones which modulate the Bragg wave field at the sea surface, and thus produce patterns of dark and bright bands recognizable as internal wave train signatures in SAR imagery.

The shape of a given internal wave signature is often dependent upon the shape of the bottom feature causing the internal wave. In all cases, the signature is a distinct set of wave packets. In the Hudson Canyon Area, where the signature appears over a ridge (Kasischke, et al., 1980) the wave packets are slightly curved and appear to be aligned such that each packet follows one after the other. In the present study where an internal wave signature appears over a seamount (IV.B.2.), the wave packets are much more curved and do not appear lined up in a row. From observations made in section IV.B.1., the effects of current shear are apparent in the wave packet.

6. Fresh-water Runoff

Fresh water runoff from rivers and estuaries is often of different temperature than the ambient ocean water.

In the Shelikof Strait area we would expect fresh-water runoff to be associated with snow melt along the Alaskan Peninsula, and we therefore expect to find cold, fresh water pools and plumes overlying warm, saline ocean water. We therefore also expect a stable atmospheric planetary boundary layer, reduced wind stress and low radar cross-section over fresh water areas. Conversely, in the ambient waters of Shelikof Strait which are warmer and saltier, we would expect a less stable planetary boundary layer, larger wind stress and therefore, brighter patterns in the SAR imagery.

A light, fresh water plume entering a nearshore area over nearly flat topography will tend to propagate offshore, but the plume will be arrested at an abrupt shelf break. Vorticity conservation across an abrupt deepening of the water column will tend to deflect the flow to the right (in the northern hemisphere), and establish a front along which the flow will proceed parallel to the shelf break in approximate geostrophic balance. This phenomenon will tend to trap fresh water plumes over flat shoals, and retain distinct areas of fresh water, the boundaries of which closely resemble the edge of the shoal. Such phenomena in SAR images may be interpreted as indicating a trend of steeply deepening bathymetry in the general location of a shoal area.

III. DATA AND METHODS

A. TEST DATA

1. SAR Imagery

SEASAT acquired the SAR imagery used in this study on three orbits over Shelikof Strait, Alaska between July 17 and August 22, 1978. Details of the system characteristics are shown in Table 2.1. The optically processed imagery of interest was obtained from the Environmental Data Information Service, National Climate Center, Room 100, World Weather Building, Washington, DC 20233, tel. (301)763-8111.

Shelikof Strait was chosen as the study area due to the availability of SAR images of the site from three separate SEASAT revolutions and because it is typical of possibly useful deep-water shipping routes. The imagery from revolution 289 on July 17 was captured on a descending path with an azimuth of 212 degrees. The site was imaged again on ascending passes on July 19 (revolution 323) with an azimuth of 328 degrees, and on August 22 (revolution 811) with an azimuth of 328 degrees (Fig. 1.1).

2. Control Data

A secondary factor in selecting Shelikof Strait as a study area was the availability of bathymetric maps of the

area. Bathymetric maps are a better data source than navigation charts for this type of study. A standard navigation chart depicts discrete depths which are representative of the soundings taken in that area. The depth represented on the chart is always the shoalest in the area, so that the actual depth for a given point may be somewhat greater than that shown. Bathymetric maps, on the other hand, are contoured directly from survey soundings (as are contour lines on topographic maps) and present a more accurate description of the bottom topography.

The control data for this study were bathymetric maps and hydrographic charts obtained from the National Ocean Survey, National Oceanic and Atmospheric Administration, Rockville, MD 20852. The three bathymetric maps covering the study area inside Shelikof Strait are Afognak (NOS No. 5-4), Iliamna (NOS No. 5-1) and Mt. Katmai (NOS No. 5-3), all at 1:250,000 scale. Historical data for these charts show hydrographic surveys covering selected subareas were performed within the past 20 years at survey scale 1:40,000 or greater, with line spacings generally less than 0.5 nautical miles (Appendix B).

The hydrographic chart used for study area VIII, southeast of Kodiak Island, is a small-scale (1:2,100,000) hydrographic chart NOS 531, titled 'Strait of Juan de Fuca to Kodiak Island,' tenth edition, printed in 1975. The hydrographic charts used for Nantucket Shoals were: NOS NO.

13237, 'Nantucket Sound and Approaches,' scale 1:80,000, 28th edition printed in 1981, and; NOS No. 13241, 'Nantucket Island,' scale 1:40,000, 11th edition published 1981.

3. Oceanographic and Meteorological Data

Oceanographic and meteorological phenomena that are relevant to this study include ocean currents, tides and tidal currents, winds, and precipitation . Some knowledge of these conditions prevailing during each observation, and an understanding of how they can affect the Bragg wave radar cross-section, is essential for ascribing SAR signatures to the proper oceanic process.

The mean current flow through Shelikof Strait was from northeast to southwest during late July and August 1978 when SEASAT acquired SAR imagery of the area. The along-shore mean current speeds ranged from 10.2 to 17.6cm/s in the upper 25 meters of the water column. (Mysak, et al., 1981 and Muench, et al., 1978)

Muench and Schumacher (1980) constructed an empirical cotidal chart for the principal lunar diurnal (M_2) tidal constituent for Kodiak Island and Shelikof Strait area (Fig. 3.1). The chart was constructed by interpolation where tide stations were closely space relative to the tidal wavelength and by estimation where tidal observations were scarce. This chart is used here in conjunction with published tidal charts for Kodiak Island to estimate the tide stage associated with each SAR image.

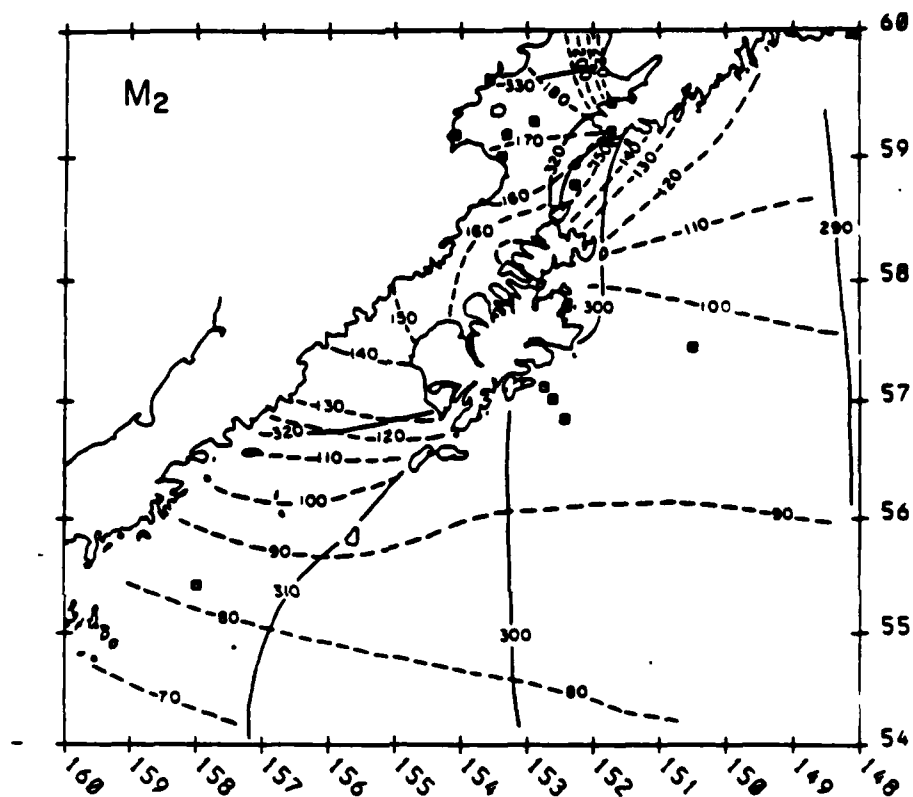


Figure 3.1. Cotidal chart for M_2 tide component. Solid lines are cophase lines referenced to Greenwich. Dashed lines are coamplitude in centimeters (Muench and Schumacher, 1980).

There are no specific wind or precipitation data available for Shelikof Strait during the times of SEASAT coverage. Some information can, however, be inferred from inspection of the images.

Localized rain squalls are more likely to affect bathymetric interpretations than a generally widespread rain storm by creating local contrasts in the radar backscatter. However, rain squalls have a very distinct SAR signature (Kasischke, et al., 1982) and the collected images do not have any of these signatures. Therefore, precipitation should not affect the bathymetric interpretations of this study.

Land topographic features affect wind stress patterns, which may in turn affect the spatial patterns of the Bragg wave radar cross-section. There are a number of along-shore areas in the Strait and a number of bays and inlets which had a low backscatter intensity in the imagery. Apparently these areas were protected from the wind by topographic features. These areas were excluded from the analysis because of the low radar return and lack of signals useful for inferring bathymetric information.

B. STUDY AREAS

The eight subareas used for analysis in this effort are shown in Figure 1.1. The subareas were selected for analysis on the basis of two criteria: 1) observed visual

signatures in the SAR imagery, and/or 2) the likelihood of finding significant wave refraction (as estimated from bathymetric maps).

The observed visual signatures in the imagery were transferred to a MYLAR overlay. The overlay was then superimposed on a bathymetric map using a zoom transfer scope by collocating topographic features (e.g. shorelines, islands, inlets). In this way, geometric distortions in the SAR imagery were corrected for and the signatures could be correlated to bathymetric features.

The wave refraction data was collected in a similar way. Once general areas of expected refraction were identified, OFT's of the areas were measured and the area of each OFT was transferred to a MYLAR overlay. Each OFT area was then colocated with the proper bathymetry using the zoom transfer scope and bathymetric maps.

In general, the areas chosen for OFT analysis had a nearly linear bottom slope. In some cases, such as Area I, the slope was fairly shallow. Area III, on the other hand, had a fairly steep slope, and the other areas fell between these two extremes.

There were two exceptions to this criteria. Area II includes a large seamount in the northeast entrance to the Strait; an attempt was made to measure the surface wave structure as it passed over the seamount, with some success (IV.B.2). In Area VIII, a large-scale natural channel

approaches Kodiak Island from the southeast. An attempt was made to locate this channel by the change in surface wavelengths as measured using the OFT, again with modest success (IV.B.8).

Originally, there were 15 areas chosen for OFT analysis. However, in seven of these areas the OFT did not yield discernible information on the surface wave structure, and therefore they were excluded from the analysis.

C. VISUAL INSPECTION OF FEATURES

1. Internal Wave Signatures

Any modulation or disturbance of the Bragg wave amplitude on the sea surface will be seen in the SAR imagery as a brightness modulation or anomaly. Previous studies have shown that major subsurface features, such as seamounts and canyons on shelf edges, often are associated with generation of internal waves with surface signatures consisting of dark and bright bands (Shuchman and Kasischke, 1979). These signatures are manifested in the imagery as wave packets radiating outward from the structure that caused the deflection. Internal waves which systematically modulate the surface radar cross-section are often generated by internal tides (Apel, et al., 1975) and other barotropic currents (Kasischke, et al., 1983) interacting with shelf breaks and other bump-like features in the bathymetry.

2. Shear

A surface wave structure incident upon an opposing surface current will be refracted against the current velocity vector, and if the current is flowing in the direction of wave propagation the waves will be pushed towards the normal to the current velocity vector (Fig. 3.2). Hence, the appearance of an apparently sheared wave structure can indicate the presence of a current. Furthermore, internal wave packet signatures extending across regions of current shear will also be distorted through differential advection.

3. Non-Linear Gravity Wave Interaction

Gravity waves propagating across broken, rough shoal areas experience non-linear interaction with the bottom. This non-linear interaction could be caused by waves crossing rocks which are classified on navigation charts as 'rocks awash' or 'uncovered' (at low tide). These interactions would cause the surface gravity waves both to break and to undergo a rapid transition from a deep-water wave to a shallow water wave. Such a rapid transition tends to strain the ultragravity wave structure, and consequently modulates the radar cross-section, producing a much higher radar backscatter over the shoal than in the surrounding area (Kasischke, et al., 1983).

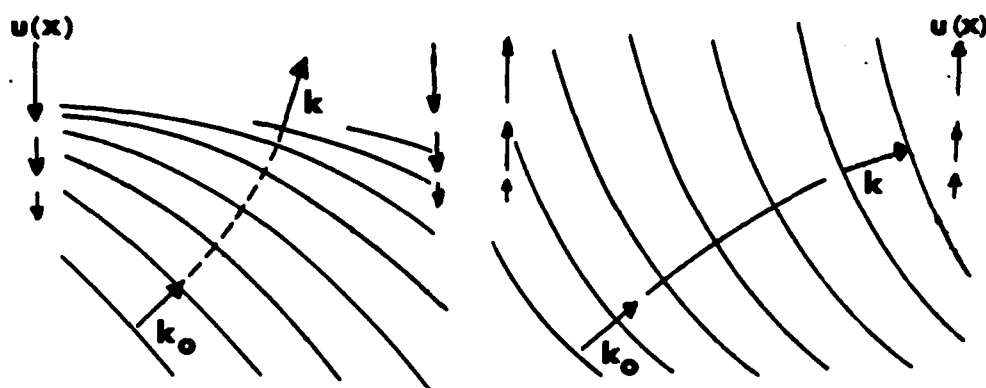


Figure 3.2. Refraction of wave structures incident upon a current (Phillips, 1981).

D. OFT ANALYSIS OF SURFACE GRAVITY WAVES

1. Wave Refraction

Linear Wave Theory is used in this study to predict water depths and shoaling using measurements obtained from OFT of SAR imagery. Linear Wave Theory in shallow water predicts that as waves propagate shoreward, wavelength decreases with decreasing water depth.

For shallow water waves where the ratio of water depth to wavelength is less than $1/25$, the water depth is related to wavelength by the equation

$$3.1 \quad d = L^2 / (T^2 g),$$

where d is water depth, L is wavelength, T is wave period and g is the gravitational constant (Coastal Engineering Research Center, 1984). For deep water waves, where the ratio of depth to wavelength is greater than $1/2$, the wave period T is given as,

$$3.2 \quad T^2 = (2\pi L_o) / g,$$

where L_o is the deep water wavelength (Coastal Engineering Research Center, 1984). The wave period remains constant, so we may substitute equation 3.2 into equation 3.1 to obtain,

$$3.3 \quad d = L^2 / (2\pi L_0).$$

Since L and L_0 can be measured from OFT of SAR images, it may be possible to determine local water depths using equation 3.3.

The change in the direction of wave propagation due to refraction can also be used to determine water depth. As waves propagate shoreward at some angle to shoaling bottom contours, they tend to turn in the direction of the shoreline as shown in Figure 3.3. Snell's Law relates the direction of propagation to the wave velocity as

$$3.4 \quad \sin \alpha_n / \sin \alpha_0 = c_n / c_0,$$

where α_0 , c_0 are deep-water direction and velocity, respectively and α_n , c_n are those at isobath depth Z_n . The change in phase speeds is related to water depth and wavelength as,

$$3.5 \quad c_n / c_0 = \tanh((2\pi d)/L),$$

(Coastal Engineering Research Center, 1984).

We may thus combine 3.4 and 3.5 to relate water depth and wavelength to propagation direction as

$$3.6 \quad \sin \alpha_n / \sin \alpha_0 = \tanh((2\pi d)/L).$$

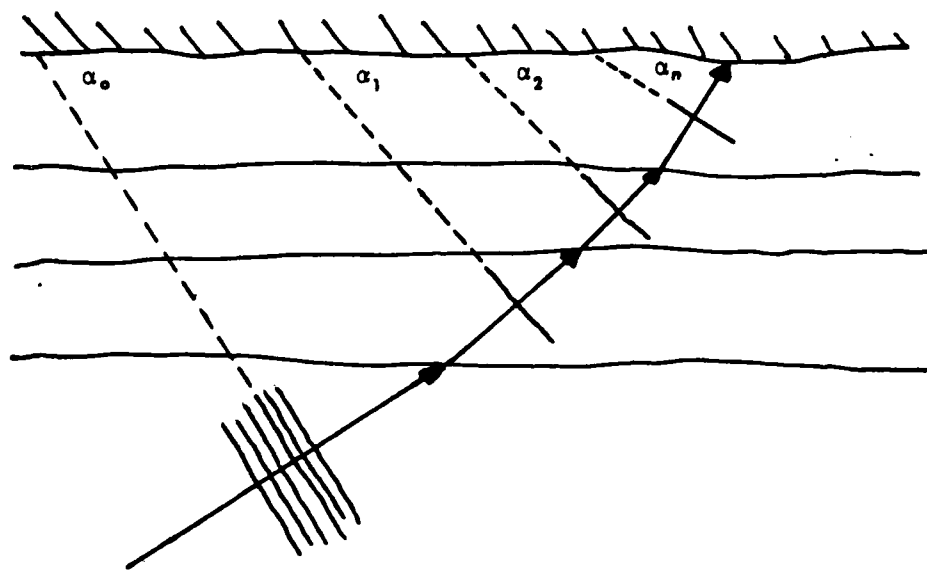


Figure 3.3. Refraction of wave structures incident upon bathymetry.

The left-hand ratio of equation 3.6 and wavelength can be obtained from OFT's of SAR images. Using that ratio and observed wavelength, water depth can be determined from empirical tables published in Shore Protection Manual (Coastal Engineering Research Center, 1984).

Equation 3.1 may also be used to measure relative shoaling. For any discrete shallow water area,

$$3.7 \quad d_1 = L_1^2 / (T^2 g).$$

And for an adjacent shoreward area,

$$3.8 \quad d_2 = L_2^2 / (T^2 g).$$

Dividing equation 3.8 by equation 3.7 yields,

$$3.9 \quad d_2 / d_1 = L_2^2 / L_1^2,$$

where L_1 and L_2 are different wavelengths of the same wave group for adjacent areas.

2. Optical Fourier Transforms

Coherent, collimated light passing first through an object transparency and then through a transform lens separates the object pattern into its Fourier components at the transform lens's focal plane (Goodman, 1968). The

Fourier components of a SAR image are thus displayed in wavenumber (\underline{k}) space and the intensity of the transform image at wavenumber (k_1, k_2) is proportional to the squared gray level amplitude of features at that vector wavenumber in the image.

The distance from the transform origin (at the focal plane) to a component is the \underline{k} -space wavenumber of that particular component. Also, the directional orientation of a component around the origin is determined by the wave's direction relative to the SAR sensor. Shuchman and Kasischke (1981) used these principles to predict water depth from OFT spectra of SAR imagery. A detailed description of the optical transform procedure is given here in Appendix A.

A helium-neon laser was used to perform the OFT's by focusing the beam through one lens onto a 1 cm^2 area of an image transparency, then through a second lens. The OFT appeared on the focal plane of the second lens and was recorded on 35 mm infrared film.

The \underline{k} -space wavenumber was then measured and mathematically transformed to the corresponding wavelength for the surface gravity wave. The angle of the component was also measured (with respect to the satellite's heading) and converted to a wave direction.

The error associated with the \underline{k} -space measurement was on the order of $\pm 1 \text{ mm}$. A geometric correction was made

for transform distortion due to the camera offset. A composite correction for errors associated with the optical train was determined empirically (Appendix A) and applied to each OFT result.

E. ASSESSMENT OF DATA QUALITY AND ERROR SOURCES

The imaging medium itself contains inherent errors. The original data was optically processed and printed on photographic film, and then copies were generated and sent to the Environmental Data Information Service (EDIS) for archival. When EDIS receives a request for imagery, they generate copies from the archived film and the user receives a third-generation film product. Moreover, in the original printing of the imagery the feed mechanism which ran the film strip through the print operation varied in its speed, creating a randomly varying distortion in the azimuth direction.

Another error source lies in the dynamic capability of the film medium. The dynamic range of the SEASAT SAR sensor was 60db. However, the photographic film's range is 17-20db. Therefore, the original data has been compressed with an ensuing loss of information (Kasischke, et al., 1980).

There are two other inconsistencies in the film medium. The first is an artificial darkening of the gray tone from one side of a subswath to the other (in the range direction). The second is a change in the scale of the

imagery, from 1:480,000 at near-range to 1:520,000 at far-range. However, both inconsistencies are insignificant at the local scale and have negligible effect on the results of this study as only a small portion of each subswath was used for each evaluation of a bathymetrically related signal.

The use of digitally-processed SAR images would not have significantly improved the accuracy of the quantitative and signature analysis using the optical techniques employed in this study. Even if the images were digitally processed, the same dynamic range restrictions would apply when the data were recorded on film to create the image. Geometric distortions in the azimuth direction would not be present; however, they were adequately compensated for in the optically-processed imagery. The other two inconsistencies noted, artificial change in tone and a changing scale, would not have been present, but as already noted, these effects were not a significant error source in the present study. On the other hand, alternative approaches using interactive digital image processing systems could take advantage of the improved dynamic range and signal-to-noise ratio inherent in the digital data.

The survey line spacings from which the bathymetric maps were compiled were generally 0.1-1.0 nautical miles (Appendix B), which transforms into 0.4-4.0 mm spacings at image scale. The area used for the OFT process was 1 cm; the

wave structure detected, therefore, could not be located more precisely than within that one square centimeter. Therefore, the survey line spacings should not have affected the OFT results.

The application of Optical Fourier Transform theory makes several assumptions: 1) that the lenses are perfectly ground, 2) that the laser beam is perfectly collimated, producing perfectly parallel rays, 3) that the focusing aperture is perfectly square, and 4) that the transparent portion of the transparency has no thickness. In this study, all of these assumptions were incorrect. In order to empirically compensate for these errors, OFT's were performed on gratings with known spacings and the predicted wavenumbers were compared to the measured wavenumber. A correction coefficient was then calculated and applied to all measured wavenumbers when calculating the corresponding wavelength. This coefficient did not correct for any distortion of the wave direction, however, which may have contributed to the relatively poor performance of wave direction changes as a depth predictor.

There were possible colocation errors associated with transferring points from the SAR image to the corresponding bathymetric map. The SAR image is a slant plane representation of a curved, three-dimensional surface, with a changing scale from near range to far range. The bathymetric map is plan view representation of a curved,

three-dimensional surface with a changing latitudinal scale. These errors were minimized by using a zoom transfer scope to perform an analog "rubber sheet" stretching to colocate identifiable features such as shorelines, swampland and islands. Because the water areas studied here are surrounded by well-defined landmarks (except for Area VIII), the colocation error was estimated to be $\leq 5\%$ of a given OFT. The uncertainty may be as high as 10% of an OFT area in Area VIII, which is outside the Strait. In no case is this a significant source of error.

IV. ANALYSIS

The SAR images, bathymetric data and oceanographic information described in Chapter 3 are analyzed in this chapter for subareas within Shelikof Strait. The case study subareas were selected according to the criteria outlined in Section III.A. This chapter will first discuss the physical environment (including bathymetry, oceanography and wind conditions) in Shelikof Strait at the times the SEASAT SAR images were acquired, and then data for the eight subareas are analyzed on a case-by-case basis.

A. OVERVIEW OF THE PHYSICAL ENVIRONMENT

1. Geographic Setting and Bathymetry

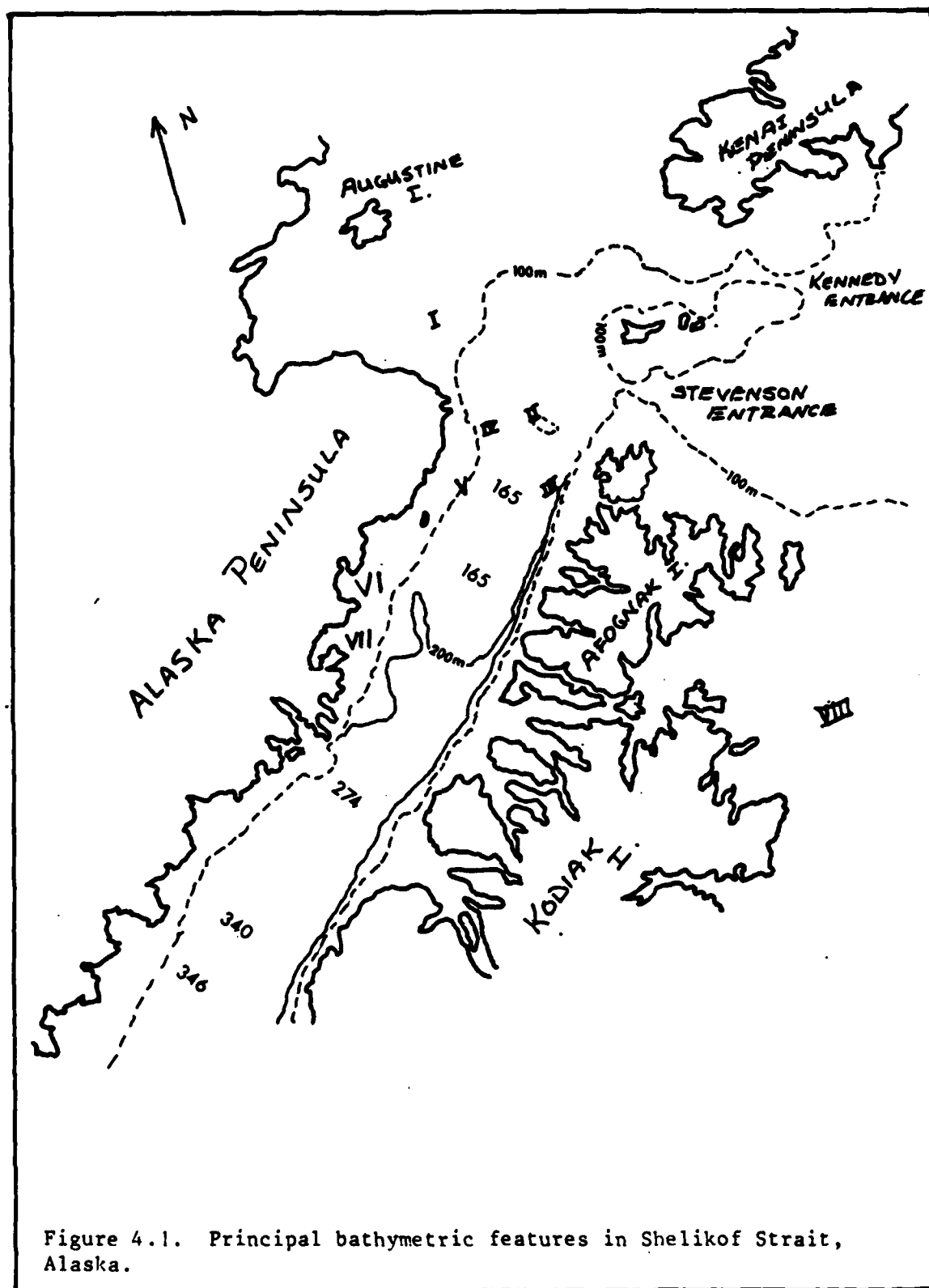
In this section, the overall bathymetric topology of the Shelikof Strait area is described, followed by a brief discussion of the relatively sparse information available on tides, tidal currents, mean current, and density stratification of the water column (including the possible influence of fresh water runoff). Finally, the prevailing wind conditions during each of the image acquisition periods are discussed, based both on synoptic scale surface wind and pressure analysis, and on visual inspection of the overall SAR images.

Shelikof Strait is located between Kodiak and Afognak Islands, and the southern coast of the Alaskan Peninsula, with a northeast-southwest orientation. The principal bathymetric features are shown in Figure 4.1.

The Strait has a depth of 196 m in the northeast entrance, increasing to 340 m in the southwest. The Strait is about 33 km wide with a generally smooth bottom, a gentle downward slope to the southeast in the upper portion of the Strait, and a slightly steeper upward slope to the southeast in the lower portion. The sides of the Strait are generally steep, shoaling from 180 to 50 m over a distance of less than 1.8 km, creating a coastal shelf with steep sides. The top of this shelf has a gentle slope and extends 5 km out from the coastline on the southeastern side of the Strait and 10 km on the northwestern side. The major submarine feature in the strait is a seamount which shoals from 160 to 100 m located in the northeastern entrance to the Strait.

2. Tides and Currents

Tidal information used in this study is derived from tide tables published by the National Ocean Survey for 1978, and from the cotidal chart in Figure 3.1 (Muench and Schumacher, 1980). All extrapolations are referred to the predicted high and low tides for the tidal station at the town of Kodiak, Alaska (Figure 1.1). The tidal stage for each image acquisition period is presented here, but no



attempt is made to generate tidal heights, due to lack of reliable tidal data inside Shelikof Strait.

The mean current in Shelikof Strait flows to the southwest, and is driven by two physical phenomena: a pressure gradient set up by the strong southwesterly flowing Alaskan Stream as it passes to the south of Kodiak Island, and a southwesterly continuation of the Kenai Current, which originates east of Kennedy and Stevenson Entrances (Fig. 4.1) (Mysak, et al., 1981). Seasonal variations in the Kenai Current cause, in turn, seasonal variations in the mean current flow through the Strait. The mean velocity through the Strait at the 25-meter depth was 10.2 cm/s in early summer 1978 and 17.6 cm/s in late summer 1978 (Mysak, et al., 1981). Further, there was a 6 cm/s current velocity associated with the M_2 tidal component superimposed on the mean flow. (Mysak, et al., 1981)

Normally, at low tide the tidal current has a reversed direction with similar velocity compared to tidal currents during high tide, and slack water occurs approximately halfway between high tide and low tide (Redfield, 1980). However, when the tidal current is superimposed on a consistent current flow, such as in Shelikof Strait, it is difficult to estimate the effects of tidal currents on net water flow during low tide, particularly in areas where the flow may interact with bathymetry. This effect may induce a 50% fluctuation in the

mean current condition during the season studied here (Mysak, et al., 1981).

The SEASAT SAR imaged the area shown in Figure 4.8 during revolution 289 at 0545 GMT on July 17, 1978. The tide tables predicted low tides for Kodiak at 0428 GMT and 1602 GMT, and high tides at 1051 GMT and 2226 GMT. It is assumed that the differences between successive high and low waters is equivalent to a 90° change in phase, and that the phase difference between Kodiak and Shelikof Strait is 20° (Figure 3.1). It is estimated that the waters inside the Strait were just approaching low tide as Seasat passed overhead, and that the mean current flow was ~ 10 cm/s to the southwest.

SEASAT acquired the SAR images shown in Figures 4.4 and 4.16 at 1430 MT on July 19, 1978 during revolution 323. The tide predictions for Kodiak were low tides at 0610 GMT and 1757 GMT and a single high tide at 1233 GMT. Thus, Shelikof Strait is estimated to have been at high tide with a mean current flow of ~ 16 cm/s to the southwest at the time the image was acquired on revolution 323.

The third image was acquired at 1700 GMT on August 22, 1978 during SEASAT revolution 811 (Figs. 4.2, 4.4, 4.7, 4.14 and 4.19). Predicted tides for Kodiak were low tides at 0919 GMT and 2156 GMT and high tides at 0315 GMT and 1539 GMT, indicating the tide inside the strait was just entering its ebb stage during this acquisition period. Again, based

on the results of Mysak, et al., (1981), the current flow is estimated to be ~18 cm/s to the southwest.

3. Density Stratification

Thermal infrared satellite images of Shelikof Strait distinguished a band of surface water that was colder than the apparent ambient waters in the rest of the strait (Mysak, et al., 1981). This band of colder water appeared along the northwestern shoreline of the strait and appeared wider in October than in January. Thus, the appearance of colder surface layers may be due to the influence of fresh water runoff, which is cold relative to the warmer, saltier ambient waters in the strait.

Although hydrological data for the Alaskan Peninsula are not available, we expect snow melt in this area to have produced a significant amount of runoff during the summer months of this study. This cold, fresh runoff would enter the Shelikof Strait from inlets along the coast. Fresh water runoff can create stationary ocean fronts over shallow water that is bounded by a sharp increase in water depth. A cold, fresh surface layer inshore of the front would produce a local increase in the atmospheric planetary boundary layer stability, so that wind stress would be greater over the ambient surface water than over the cold fresh water area. This would cause an abrupt change in the radar cross-section and hence, the ambient waters would appear brighter in SAR imagery than would the colder, less saline waters. Some

examples consistent with this paradigm occur in the images studied here.

4. Wind Conditions

There is no local wind data available for the areas of interest within Shelikof Strait. Therefore, wind conditions are estimated from National Meteorological Center (NMC) Final Analysis data for the SEASAT acquisition periods used in this study.

The data for July 17, 1978 (SEASAT revolution 289) indicate winds were moderate from the northeast. Thus, the wind stress was roughly aligned along the axis of Shelikof Strait. Therefore, topographic effects on wind patterns over the strait should have been minimal.

The data for July 19 and August 22, 1978 (SEASAT revolutions 323 and 811, respectively) indicate winds were moderate from the southeast, a 310° bearing. The wind patterns were most certainly altered by topography as they crossed Kodiak and Afognak Islands and as they approached the mountainous topography of the Alaskan Peninsula.

B. CASE STUDIES OF LOCAL SUBAREAS

The SAR imagery contains organized patterns of radar cross-section returns throughout the study area. Four subareas in and around Shelikof Strait were chosen for analysis based on macro-scale radar brightness features in the SAR imagery. Internal wave signatures are visible in

the images of subareas I, II and VII. Also, brightness anomalies are also visible in subareas II, III, IV, VI and VII.

Four other subareas, Areas III, IV, V and VIII, were selected for OFT analysis based on the expected wave refraction as determined from bathymetric maps of the area. OFT analysis was also done on the subareas chosen from visual inspection of the imagery. The location of the eight case study subareas are indicated in Figures 1.1 and 4.1.

1. Area I: Internal Waves and Surface Gravity Wave Refraction

Area I lies between Shelikof Strait and the mouth of Cook Inlet, (Figure 1.1). The imagery analyzed for this subarea was acquired during revolution 811 just before high tide, (1700 GMT July 19, 1978). There were moderate, southeasterly winds in the area during acquisition.

The transform areas are not close to shore and the internal wave signature approaches Augustine Island from approximately the same direction as the wind. Coastal topography should not have caused large variations in the down-strait wind pattern, and therefore, should not have strongly influenced the patterns of wind-induced radar cross-section in the SAR imagery.

Figure 4.2 shows an internal wave signature in the form of a wave packet propagating toward Augustine Island, beginning approximately ten km offshore with a heading of



Figure 4.2. Imagery from revolution 811 covering Area I, showing transform areas B14, B15 and B16.

320° with wavelengths decreasing from 1.7 to 1.0 km. There is a slight northwest shear in the wave structure, which is an indication of an incoming current. As the tide is still approaching high water, the internal waves are possibly incident upon the incoming tidal current (Phillips, 1981).

The internal wave packet appears in water with a depth of 45 m where the bottom slope is very small (almost a plateau) and continues to the island's shelf. The wave packet is indicated by curved parallel lines in Figure 4.3. Going seaward, the bottom's downward slope begins to steepen at around the 60 m curve and increases drastically at the 75 m curve (Fig. 4.3). The steeper slope may be reflective and turning the internal waves back toward deeper water and down, with no interaction with the surface and no SAR signature. Shoreward of the 60 m curve the slope is very gradual, and may be horizontally transmissive.

The internal wave signature wavelength decreases and brightness contrast increases as the wave approaches the more steeply sloping bottom near Augustine Island (Fig. 4.3). These observed characteristics of the wavetrain, e.g., change in wavelength and increased amplitude, are consistent with theory (Wunsch, 1968). Also, the observed curvature in refraction is consistent with curvature in the bathymetry.

The bathymetric maps show a large number of rocks awash near and to the south of Augustine Island, as well as

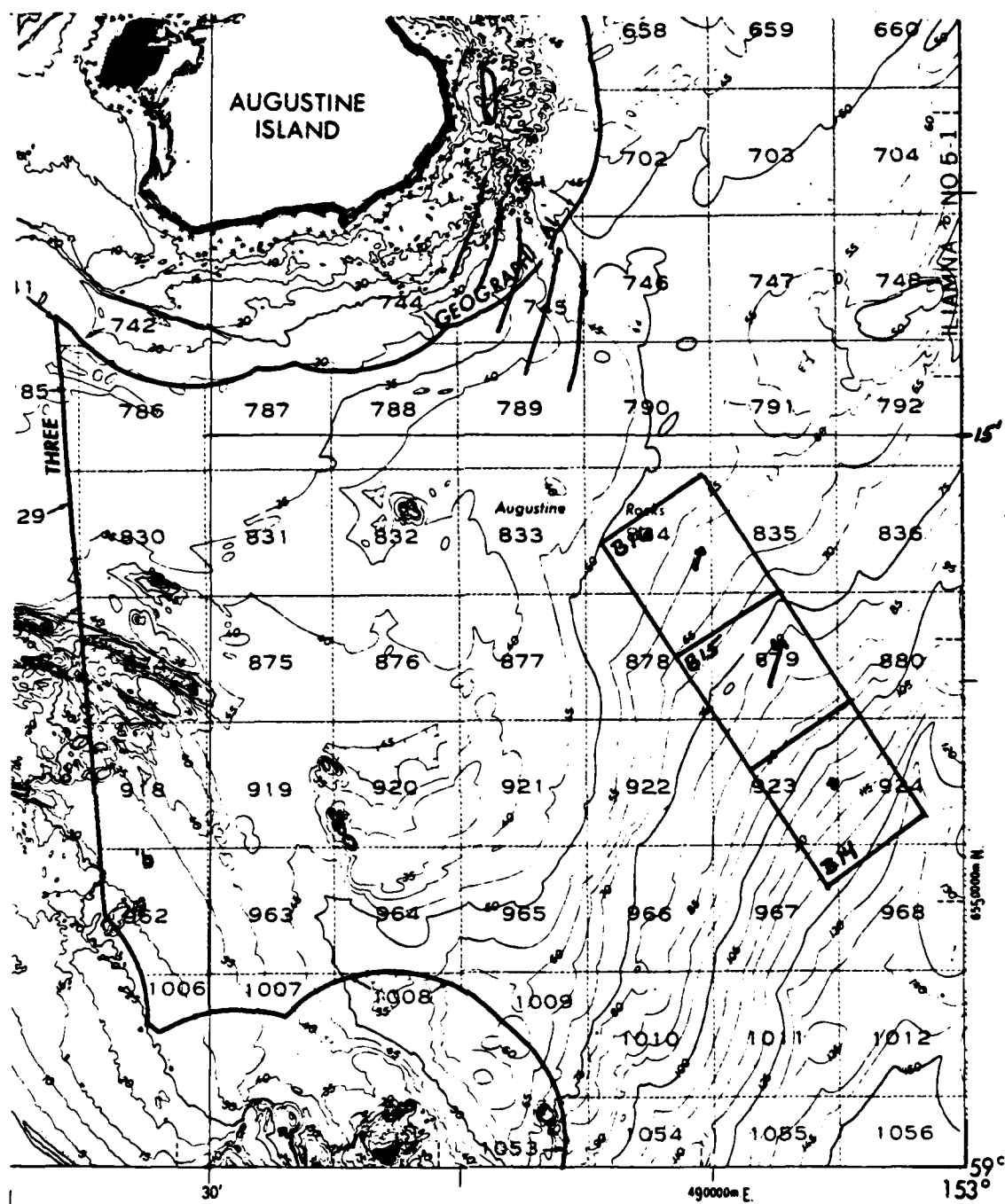


Figure 4.3. Bathymetry of Area I, (depths in meters, scale 1:250,000).

a rough, broken bottom to the east of the island. These features should have produced distinct signatures in the form of brightness anomalies in the imagery. However, only one signature appeared; a small, elongated patch east of the island. Tidal heights in this area are typically tens of meters in magnitude and the water level was approaching high tide during the acquisition period. Hence, lack of signatures in the SAR image may be due to too much water over these features, preventing detectable modulation of the surface radar cross-section. This possibility clearly suggests the advantages of obtaining several SAR images of a study area at different tidal stages in future research and applications. Whatever the reason, there was no indication of these known shoals in the SAR image. This negative finding highlights the one-sided nature of SAR information; it can be trusted to indicate the possible (even probable) presence of shoals, but it can not be trusted to definitively indicate the absence of shoals.

Ten OFT's were generated for analysis in this subarea. However, only three yielded measurable information, indicating that if there was a dominant wave structure in most transform areas, it had no components discernible to the OFT process.

The three transforms which showed a discernible dominant wavenumber (B14, B15, and B16), are in the areas delineated in Figure 4.3, and the measured wavelengths and

directions are given in Table 4.1. The spatial relation of the transforms and the large differences in measured wavelengths indicate the OFT's measured a different wave structure in each transform area. Even though a dominant wavelength was discernible in each OFT of Table 4.1, all evidence suggests that gravity waves in this area were of extremely low amplitude and are therefore unsuited for detection of wave refraction effects.

Table 4.1. Wavelengths and Directions in Area I

Transform Area	L(m)	α (degrees)
B14	378+9	348+0.5
B15	1,825+243	18+2.0
B16	935+65	20+1.0

2. Area II: Internal Waves, Brightness Anomalies and Surface Gravity Wave Refraction

Area II is located in the northeastern entrance of Shelikof Strait. Figure 4.4 shows the imagery acquired during SEASAT revolution 811 covering this area and Figures 4.5 and 4.6 show the bathymetry.

Synoptic wind analysis shows the winds during this acquisition period (August 22) were moderate and from the southeast, coming into the subarea across Afognak Island and through Kennedy and Stevenson Entrances. There does not appear to be any low radar return areas along the shoreline at the southeastern edge of Figure 4.4, which would be



Figure 4.4. Imagery from revolution 811 covering Areas II, III and IV, showing transform areas A4, A5, A8, A22, A23, A26, A27, A30 and A31.

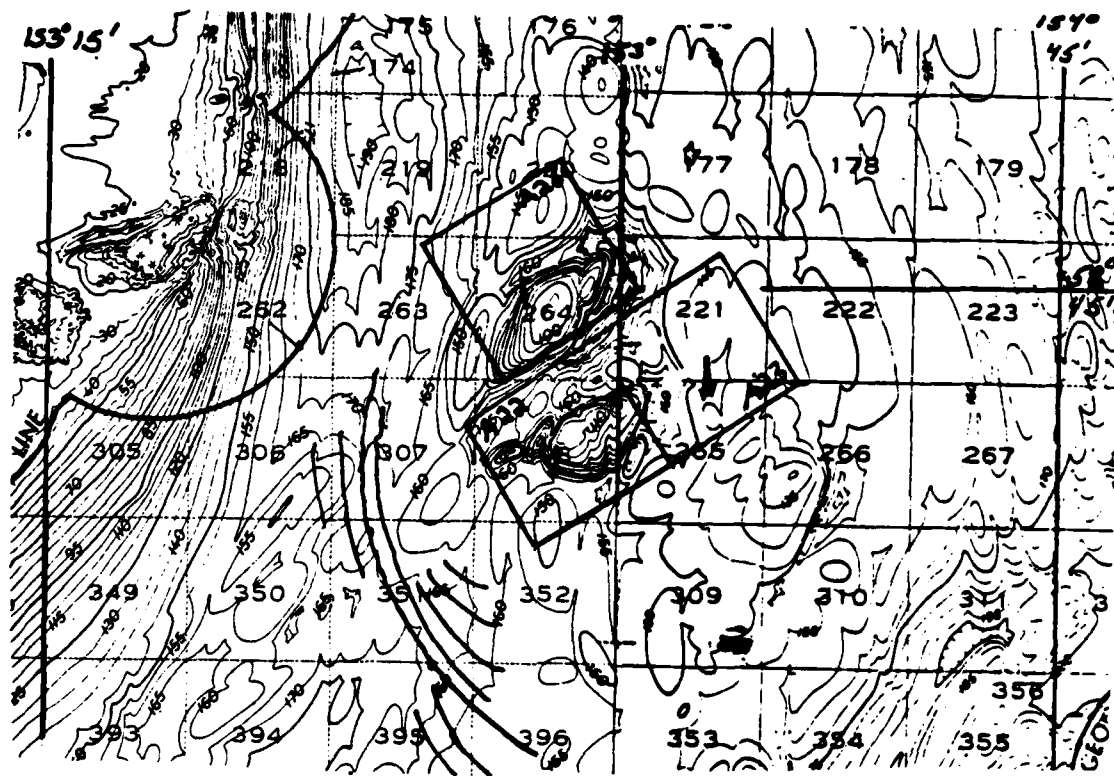


Figure 4.5. Bathymetry of Area II (depths in meters, scale 1:250,000).

indicative of a lee area, suggesting that local wind patterns do not make an important contribution to the features seen in this image.

There are internal wave signatures in the form of wave packets in the imagery which correspond to a seamount, seen in the bathymetry near 58°45'N, 153°W. The depth in the area of the signatures is approximately 210 m, shoaling to 70 m over the seamount. The spatial offset of the signatures from the seamount resembles offsets found in similar circumstances by Shuchman and Kasischke, (1979).

Mysak, et al., (1981) have shown that the density distribution within Shelikof Strait can be approximated with a two-layer model, where the upper layer varies in depth from 25 to 90 m. The internal wavelength as measured from its SAR signature in Area II was 900 m. The height for the upper layer (h_1) is 90 m and for the bottom layer (h_2), 80 m. The wavelength (L) is much larger than the heights, hence, the wave group velocity,

$$c = \frac{(\rho_2 - \rho_1)(g/k)}{\rho_2 \coth(kh_2) + \rho_1 \coth(kh_1)} ,$$

can be reduced to ,

$$c = \frac{gh_1h_2}{h_2 + h_1} \left(1 - \frac{\rho_1}{\rho_2} \right)$$

where

$$1 - \frac{\rho_1}{\rho_2} = 0.002 \text{ (Knauss, 1978).}$$

Thus,

$$4.1 \quad C = 0.002 \frac{gh_1h_2}{h_2 + h_1}.$$

Using equation 4.1 and the water layer heights determined from Figure 4.5, the internal wave group velocity is, $C = 2.7 \text{ km/hr.}$

The leading wave is 12 km from the top of the seamount shown in Figure 4.5. Assuming the internal wave generated at the seamount through interaction with the incoming tide, the internal wave required five hours to reach its present position; this is consistent with the estimated tidal phase.

In addition to the internal wave signatures, the SAR image displays a brightness anomaly directly over the seamount. Because the seamount is in the center of the strait, it is unlikely that this pattern could result from wind variance. Therefore, the increase in radar cross-section must be associated with some current-wave interaction over the shoal. One possible explanation is an interaction between the strong prevailing southwest current and the seamount, which is not a single conical shape, but two cone-like structures rising 70 m above and to either side of a small canyon. Also, the slope is much steeper on the down-current side of the seamount than on the up-current

side. This bathymetry (and its interaction with the current) may have modified the surface radar cross-section, increasing the backscatter intensity seen in the SAR image.

The brightness anomaly seen in figure 4.5 correlates nicely with the location of the seamount. Unfortunately, the imagery acquired during SEASAT revolution 289, which covered the same area, had such high levels of backscatter intensity throughout the area that no information can be obtained from it (i.e., the area was saturated).

Table 4.2. Wavelengths and Directions in Area II

Transform Area	L(m)	α (degrees)
A22	845+51	180+0.0
A23	1,160+89	175+0.5
	1,024+76	178+1.0
A26	856+51	170+1.0

Three OFT were generated for the surface wave structure over the seamount. The locations of the transforms (A22, A23 and A26), are shown in Figure 4.5 and Table 4.2 shows the measured wavelengths and directions.

Transform A23 has two measurable components which may indicate a wave structure undergoing refraction as it propagates over a shoaling bottom; the wavelength shortening and the direction change is consistent with the bathymetry shown. However, the error associated with measuring wavelengths of this magnitude makes it difficult to compare similar wavelengths, the one mm standard error of

measurement affects small wavenumbers much more than large wavenumbers. Hence, the best that can be predicted for transform area A23 from OFT analysis is shoaler water in the westernmost portion of the area.

There are two cases where depth range and a shoaling ratio can be predicted; OFT data from A23 and A22 were used to predict depths and shoaling ratios in A22, and data from A26 and A22 were also used to predict depths and shoaling ratios in A22. The ratio of d/L here is larger than $1/25$. Therefore, the area should be classified as transitional water and the following equation from the Coastal Engineering Research Center (1984) used,

$$4.2 \quad L = (gT^2)/(2\pi)(\tanh(2\pi d/L)).$$

From the bathymetry, the depths in area A23 range from 125 to 160 m with an effective median depth of 145 m. Using equation 4.2 and the measured wavelength from A23, $L_{23}=1,160$ m, the wave period (T) is calculated to be 36 sec for a depth of 125 m, and a depth of 62 m is predicted for area A22. Using the same data, but a depth of 160 m in A23, the wave period (T) is calculated to be 33 sec, predicting a depth of 76 m in area A22, giving a predicted depth range of 62 to 76 m in area A22. A predicted effective median depth of 70 m was also calculated using the effective median depth and the measured wavelengths for A23 in equation 4.2. The

actual depth range in area A22 as shown in the bathymetric map is 110 to 160 m with an effective median depth of 135 m, a 48-percent error in the predicted median depth.

Similarly, using OFT data from A26, a predicted depth range of 94 to 148 m and an effective median depth of 144 m was calculated for A22, a 7-percent error in the predicted median depth. The apparent reason for the improvement in accuracy is that the path from A26 to A22 follows a ray path, A23 to A22 parallels the apparent ray path.

3. Area III: Brightness Anomalies and Surface Gravity Wave Refraction

Area III is located south of the seamount discussed above, and Figure 4.4 shows the imagery of this area acquired during Revolution 811. Figure 4.6 shows the bathymetry for this area and the wavelengths and directions for the three transforms developed from the imagery (A4, A5 and A8) are listed in Table 4.3. Note that all transforms have more than one distinct wavenumber component, but Figure 4.6 shows only one arrow for clarity.

There are some scalloped bands of brightness off Raspberry Island (labelled A in Figure 4.6) and off Afognak Island (labelled B in Figure 4.6) in the lower portion of the imagery shown in Figure 4.4. These anomalies may be interpreted as indicators of the escarpment shown in the bathymetric map, even though feature A is 2.5 km and feature B is 10.0 km from the escarpment. Although the mechanisms

which produce the anomalies are unclear, that uncertainty would not preclude taking advantage of the fact that the shapes of anomalies are indicative of the trend of nearby bathymetry.

Table 4.3. Wavelengths and Directions in Area III

Transform Area	L(m)	α (degrees)
A4	1,021+76	184+0.0
	1,116+91	186+0.5
	1,150+96	181+0.0
A5	1,010+70	174+0.5
	1,342+124	175+1.0
	857+49	170+1.0
A8	2,285+385	190+1.0
	2,362+413	189+1.0

Wave refraction data obtained from OFT's were used to predict a water depth range for transform area A4 using the previously described method. The depth ranges in A5 and A4 are 170 to 200 m and 50 to 200 m, respectively and the wavelengths were 1,342 m and 1,150 m, respectively. The effective median depths for A5 and A4 are 190 m and 150 m, respectively. Thus, the predicted depth range in area A4 is 117 to 135 m with a predicted effective median depth of 130 m, an error of 13-percent.

4. Area IV: Brightness Anomalies and Surface Gravity Wave Refraction

Area IV is in the northern corner of the upper entrance to Shelikof Strait, (Fig. 1.1). The bathymetry and

transform areas are shown in Figure 4.7. Figure 4.4 shows a large, bright area in the imagery to the southwest of the three transform areas, which corresponds to an extremely shoal area with rocks awash, (Fig. 4.7). The imagery shows a fairly rough surface, possibly caused by water crossing the submerged rocks at high tide.

Table 4.4 lists the wavelength and directions measured from the OFT's in transform areas A27, A30 and A31. Note that area A31 has two wave components, but Figure 4.7 shows only one arrow for graphical clarity.

Table 4.4. Wavelengths and Directions in Area IV

Transform Area	L(m)	α (degrees)
A27	970+65	179+0.5
A30	845+49	173+0.5
	836+48	182+0.5
A31	799+46	178+0.0
	784+44	177+0.5

Depth ranges and effective median depths were predicted for area A30 using OFT data from areas A30 and A27, and for area A31 using OFT data from areas A30 and A31. The depth range in area A27 is 150 to 185 m with an effective median depth of 170 m, and the range in A30 is 50 to 190 m with an effective median depth of 135 m. Thus, using 970 m and 836 m for the measured wavelengths in areas A27 and A30, respectively, a predicted depth range of 102 to 120 m with an effective median depth of 113 m was calculated for area A30. When compared to the actual effective median

153° 30'

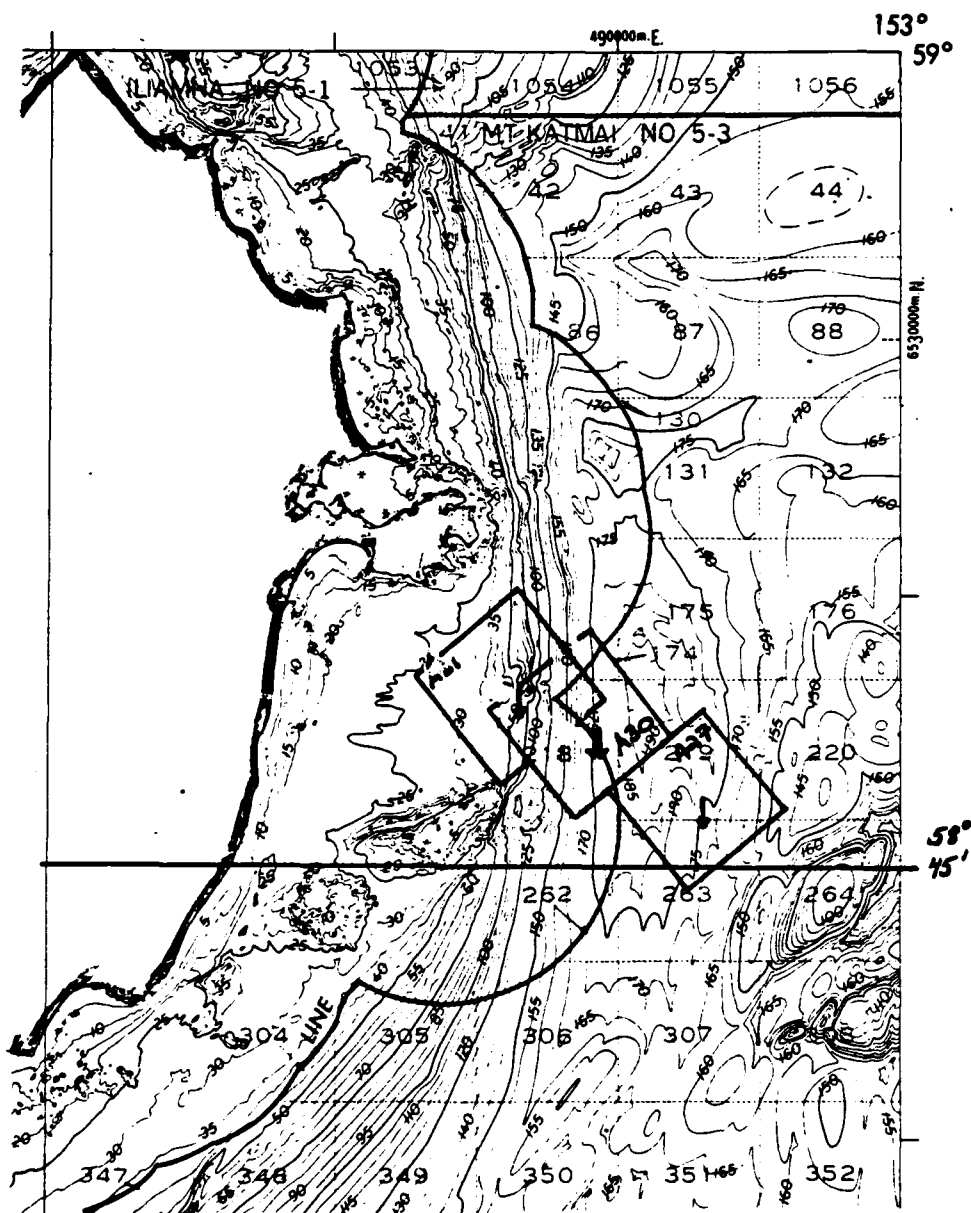


Figure 4.7. Bathymetry of Area IV, (depths in meters, scale 1:250,000).

depth, the prediction has a 16-percent error. The observed change in wave direction is consistent with the bathymetry.

The depth range in transform area A31 is 30 to 175 m with an effective median depth of 102 m. The predicted depth range is 44 to 151 m with a predicted effective median depth of 113 m, an error of 11-percent. The small error in the predicted depth range for area A31 is likely due to the large spatial overlap between the two transform areas.

The waves in this area are propagating alongshore, rather than onshore and the wavelengths in transform area A31 may be due to the effects of shoaling which occurred somewhere to the north. Before shoaling occurred, off the image to the north, the deep water wavelength which refracted to that shown in A31 was presumably similar to that observed in the deeper water of transform area A27.

5. Area V: Brightness Anomalies and Surface Gravity Wave Refraction

Area V is located along the northern edge of the Strait, (Fig. 1.1). Figures 4.8, 4.9 and 4.12 show the imagery of the area from all three orbital passes. This area was covered by SAR images acquired during three different revolutions. As such, it is the only multi-temporal case in this study. One of the images (Fig. 4.9) had such high intensity radar returns that visual interpretation was impossible. However, there are similar

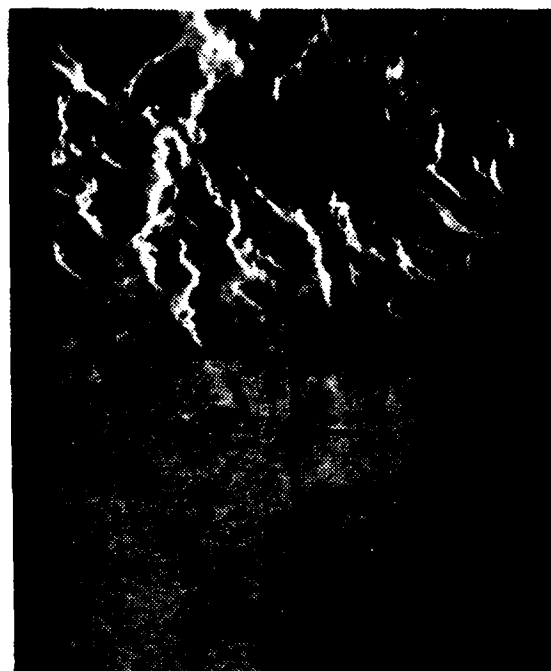


Figure 4.8. Imagery from revolution 811 covering Area V, showing transform areas D17 and D16.

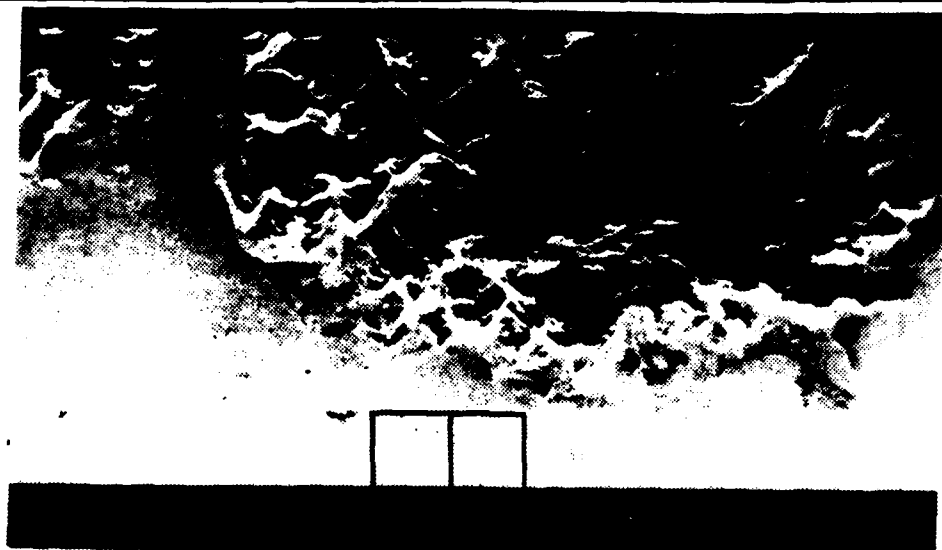


Figure 4.9. Imagery from revolution 289 covering Area V, showing transform areas G1 and G2.

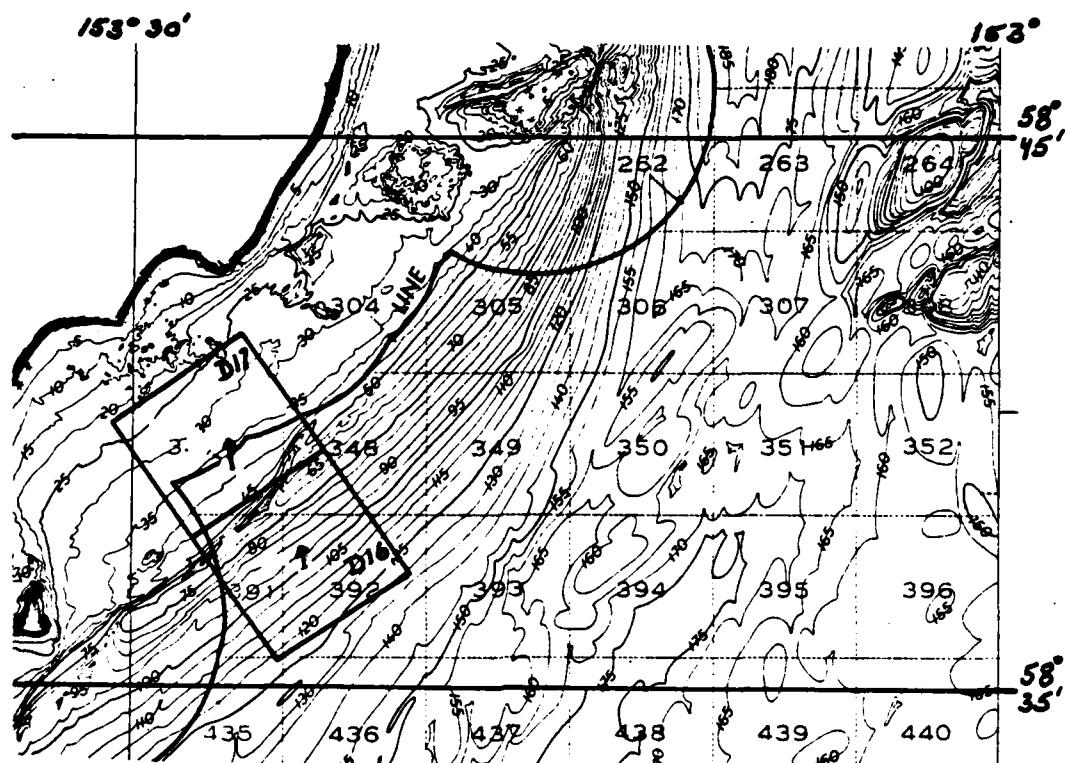


Figure 4.10. Bathymetry of Area V, with transform areas D17 and D16, (depths in meters, scale 1:250,000)

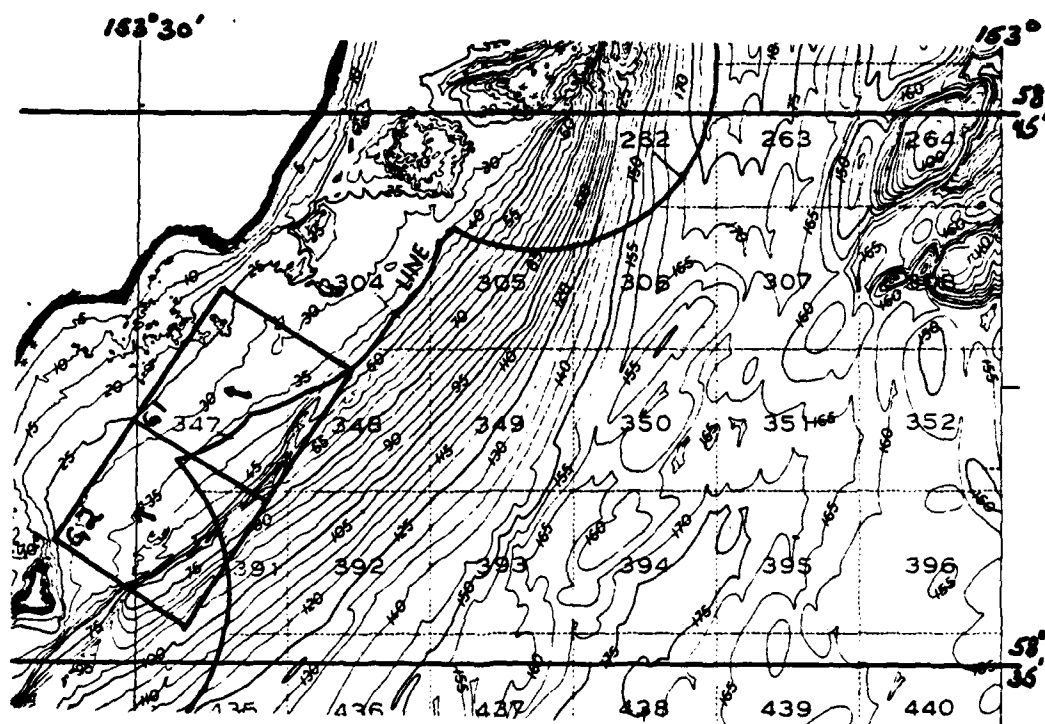


Figure 4.11. Bathymetry of Area V, with transform areas G1 and G2, (depths in meters, scale 1:250,000).



Figure 4.12. Imagery from revolution 323 covering Area V, showing transform areas F1, F2 and F4.

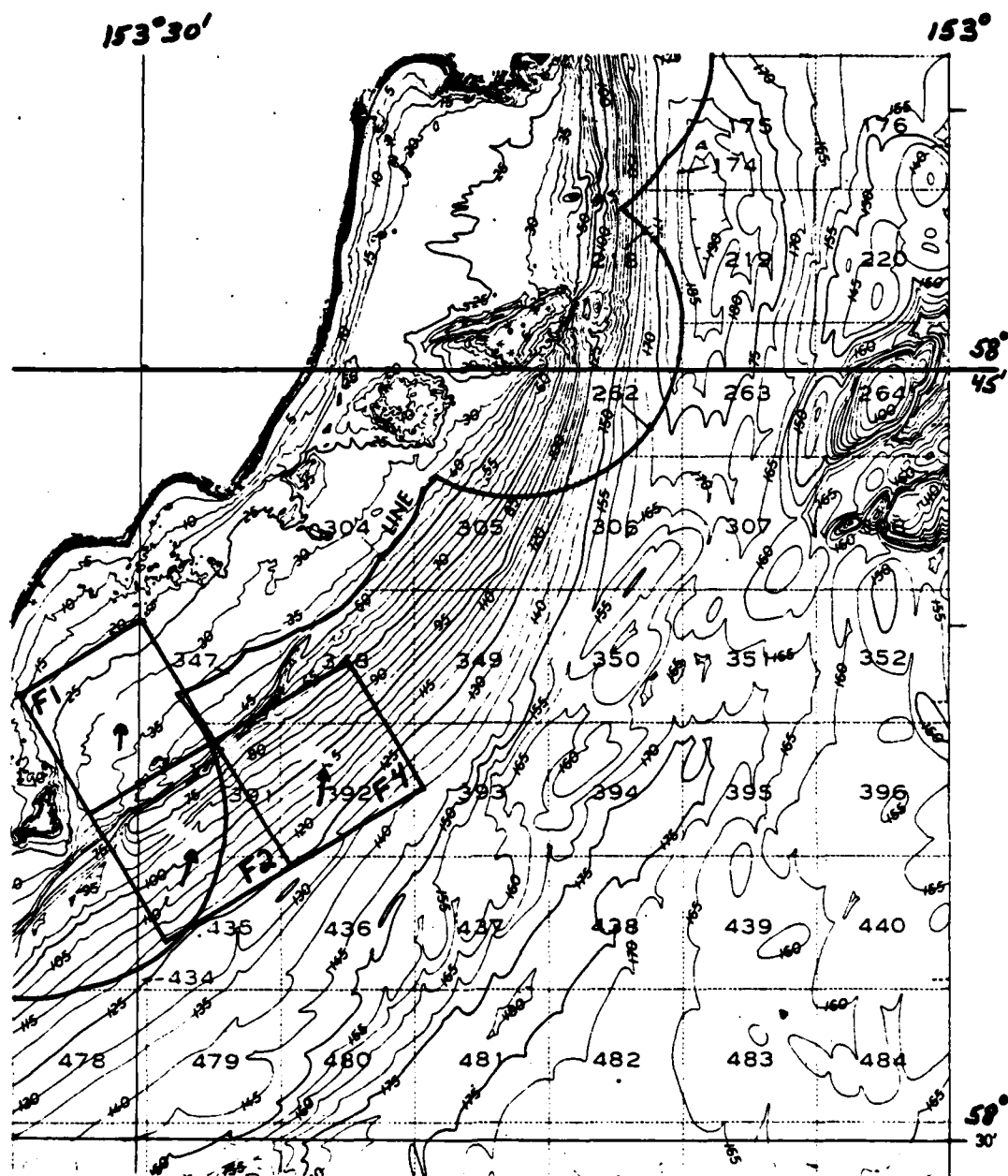


Figure 4.13. Bathymetry of Area V, with transform areas F1, F2 and F4, (depths in meters, scale 1:250,000).

brightness anomalies in Figures 4.8 and 4.12 which appear to be related to the same bathymetric feature.

There is an elongated brightness anomaly in Figure 4.12 which corresponds to the shoaling area shown between $58^{\circ}44'N$ and $58^{\circ}45'N$ at $153^{\circ}W$ longitude in Figure 4.10. Portions of a similar-shaped anomaly can also be seen in Figure 4.9, although that anomaly is partially obscured by a large-scale cyclonic eddy feature. Winds are moderate and southeasterly; therefore, the mountains along the shoreline may be forcing part of the air flow along the shore, straining the surface radar cross-section such that a cyclonic brightness anomaly appears in the imagery.

Figures 4.10, 4.11 and 4.13 show the corresponding bathymetry and transform areas and Table 4.5 lists the wavelengths and directions measured from the transforms. Note that transform D17 has two measured wave components, but Figure 4.10 shows only one for clarity.

The relationship between measured wavelengths for transform areas D17 and D16 is reversed from the expected relationship. Figure 4.10 shows D17 is over shoaler water than D16, but has longer wavelengths. This anomaly is not explained by the uncertainty in the measurements; therefore, the transforms must be showing two separate wave structures. The spatial relationship of the two transform areas and the

shoreline makes it unreasonable to accept the two wavelengths as part of the same wavetrain.

Table 4.5. Wavelengths and Directions in Area V

Transform Area	L(m)	α (degrees)
D17	902+61	358+0.0
	891+58	353+0.5
D16	588+24	346+0.5
G1	796+37	284+2.0
G2	699+25	292+2.0
F1	722+37	4+0.0
F2	1,229+106	19+1.0
F4	1,106+88	9+0.5

The predicted depth range for transform area G2, using OFT data from G1 and G2, is 19 to 49 m with a predicted effective median depth of 31 m. The actual depth range for G1 is 25 to 65 m with an effective median depth of 40 m, and 30 to 75 m with an effective median depth of 35 m for G2, showing the predicted effective median depth has an 11-percent error.

The change in wave direction from G1 to G2 is clockwise, indicating bathymetric contours oriented along a general northeast-southwest axis, which is consistent with the bathymetry in Figure 4.11.

The depth ranges in transform areas F1, F2 and F4 are 20 to 45 m, 50 to 125 m and 65 to 135 m, respectively with effective median depths of 32, 95 and 97 m, respectively. The predicted depth range for area F1 using data from F2 is 17 to 40 m with a predicted effective median

depth of 31 m, a 3-percent error. Data from transform area F2 were also used to predict a depth range and an effective median depth in area F4. The predicted depth range in F4 is 40 to 99 m with an effective median depth of 76 m, an error of 22-percent. The differences in wavelengths and wave directions between transform areas F1, F2 and F4 are consistent with the bathymetry, i.e., the wave directions are turning towards the normal to the bathymetry and the wavelengths are shortening as the wavetrain propagates shoreward.

6. Area VI: Brightness Anomalies and Surface Gravity

Area VI is located along the northwest shelf of Shelikof Strait (Fig. 1.1). Figure 4.15 shows the area's bathymetry and Figure 4.14 shows the imagery. Table 4.6 lists the measured wavelengths and directions.

A small elongated patch of high reflectivity appears in the bay located in the upper right corner of the imagery (outlined area in Figure 4.14). This brightness anomaly correlates directly to the broken, irregular bathymetry shown in Figure 4.15. There are also some brightness anomalies near the shoreline on the extreme left edge of the image in Figure 4.14 which correspond to the rough bottom shown in Figure 4.15.

The dark areas which parallel the embayments to the north of the transform areas may be due to one of two conditions. These areas may be protected from the local

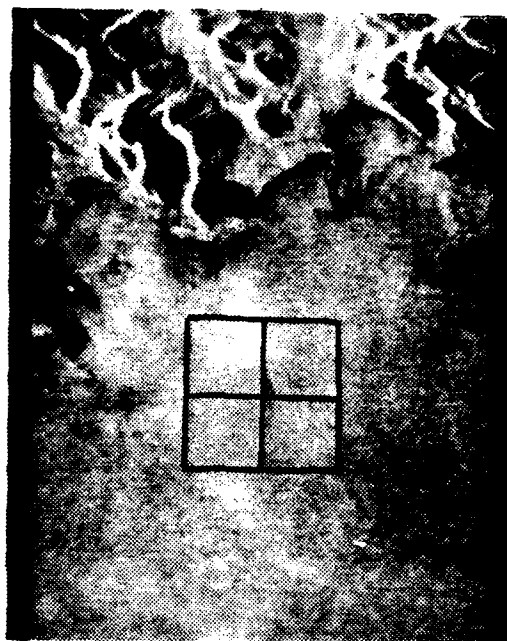


Figure 4.14. Imagery from revolution 811 covering Area VI, showing transform areas C6, C7, C8 and C9.

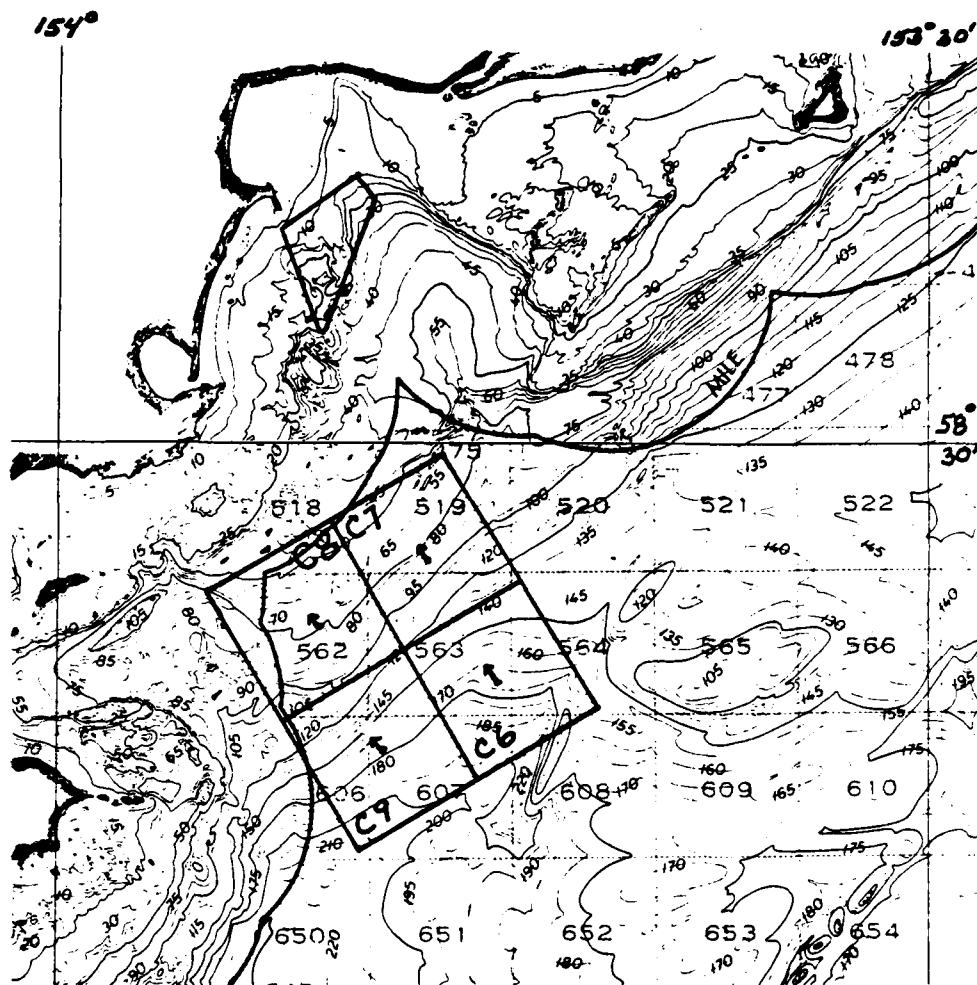


Figure 4.15. Bathymetry of Area VI, (depths in meters, scale 1:250,000).

wind patterns (even though synoptic winds are southeasterly, making this an unlikely explanation); or they may be due to the influence of fresh water entering the strait from rivers.

Table 4.6. Wavelengths and Directions in Area VI

Transform Area	L(m)	α (degrees)
C6	838+44	326+2.0
C7	658+25	326+1.6
C8	533+14	325+1.0
C9	543+19	323+1.0

Depth ranges and effective median depths were predicted for transform areas C8 and C7. Data from area C9, with a depth range of 120 to 200 m and an effective median depth of 170 m, were used to calculate the predictions for C8. The predicted depth range for C8 is 108 to 153 m with a predicted effective median depth of 150 m compared to the actual depth range of 45 to 110 m and effective median depth of 80 m, an 88-percent error.

The predicted depth range for area C7 was calculated using data from area C6, which has a depth range of 140 to 195 m and an effective median depth of 170 m. The predicted depth range of 75 to 99 m and predicted effective median depth of 85 m has a 6-percent error when compared to the actual depth range of 45 to 135 m with effective median depth of 90 m.

AD-A161 181

DETECTION OF SHOALS IN SEASAT SYNTHETIC APERTURE RADAR
IMAGERY. SELECTED CASE STUDIES(U) NAVAL POSTGRADUATE
SCHOOL MONTEREY CA R L DICKERMAN SEP 85

272

UNCLASSIFIED

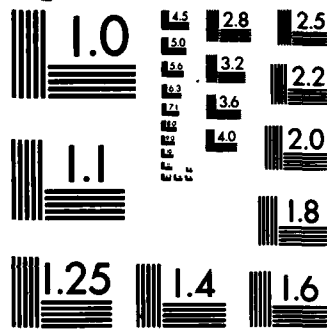
F/G 8/10

NL

END

FILMED

D1AC



MICROCOPY RESOLUTION TEST CHART
NATIONAL BUREAU OF STANDARDS-1963-A

The measured wavelength differences between the four transform areas, C6, C7, C8 and C9, are consistent with the bathymetry shown in Figure 4.15. The very small changes in wave direction are consistent with waves propagating normal to the shoaling isobaths.

7. Area VII: Brightness Anomalies and Density Stratification

Area VII is located at the mouth of Kukak Bay (Fig. 1.1). Figure 4.16 shows the imagery for the area and Figure 4.17 shows the corresponding bathymetry. This area has the most dramatic brightness anomalies in this study. Because of the large modulations in the radar cross-section, this image is unsuitable for OFT analysis. Therefore, no attempt was made to interpret this image in terms of surface gravity wave refraction.

There are a number of anomalies in the image in Figure 4.16 which appear to be related to bathymetric features shown in Figure 4.17. The largest anomaly (labelled A in Figure 4.17) is a sharp break in the image brightness, with high backscatter intensity on one side and very low intensity on the other. The bathymetry shows a small seamount less than 2.0 km upstream from the anomaly. The seamount sits at the mouth of a small submarine canyon with depths sloping from 250 to 150 m upstream of the feature and a fairly flat bottom with depths to 270 m on the downstream side. The feature has three peaks with charted

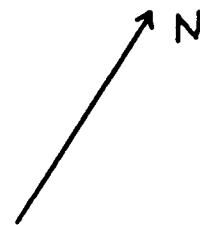


Figure 4.16. Imagery from revolution 323 covering Area VII.

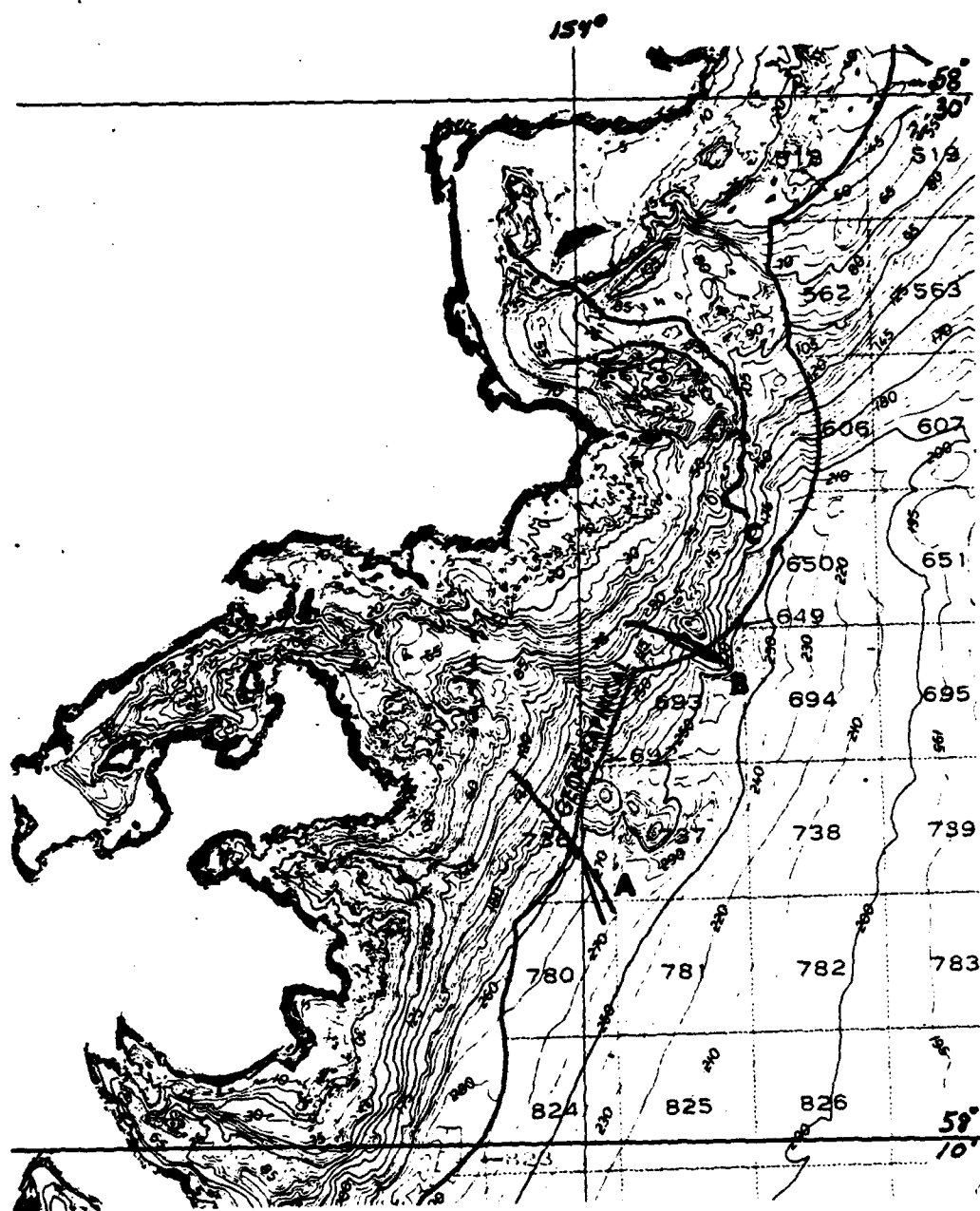


Figure 4.17. Bathymetry of Area VII, (depths in meters, scale 1:250,000).

depths of 170, 190 and 140 m respectively, progressing shoreward.

These patterns could be the result of water column stratification due to fresh-water runoff. The cold, fresh surface water layer would stabilize the atmospheric planetary boundary layer relative to the warmer, saltier surface water layer in the strait, producing a marked difference in the image brightness (due to the radar cross-section modulations) over the two different water masses. There are also internal wave signatures at the southeastern portion of the intensity break, the appearance of which is also characteristic of fresh-water runoff fronts where abrupt changes in stratification may occur (e.g., see Fig. 34 of Fu and Holt, 1982).

A second, smaller anomaly is located 500 m downstream from another, smaller seamount (marked B in Figure 4.17). The second seamount rises approximately 100 m from the base. The anomalous signature from feature B is offset from the seamount, and resembles the pseudo-imaging of bottom relief similar to that found in Nantucket Shoals SAR imagery.

Depths across Nantucket Shoals are generally less than 25 m, but the depths in this area range from 75 to 170 m. This would indicate that the processes discussed in section II.B.3 may be valid for depths of 100 m or more, as

well as for the shallower depths found near Nantucket Shoals.

There is a long, bright anomalous line located in the upper right-hand corner of the image in Figure 4.16. This anomaly (labelled C in Figure 4.17) is roughly located along a shelf break inshore of a narrow submarine canyon, and may be another example of a shelf break trapping a lens of cold, fresh-water runoff.

8. Area VIII: Surface Gravity Wave Refraction

Area VIII lies outside Shelikof Strait, to the southeast of Kodiak Island and was chosen in an attempt to

Table 4.7. Wavelengths and Directions in Area VIII

Transform Area	L(m)	α (degrees)
K3	866+38	229+2.0
K4	923+60	179+0.5
K5	1,165+88	181+0.3
K6	1,075+76	182+0.5
K7	1,271+110	179+0.5
K19	886+55	176+0.5
K20	1,068+72	167+0.5
K21	1,388+131	164+2.5

locate the channel seen in Figure 4.18 on the basis of wave refraction. A number of OFT's were attempted throughout the channel, and eight had distinct dominant wave numbers. The wavelengths and directions for the transform areas are listed in Table 4.7 and Figure 4.19 shows the imagery for the area.

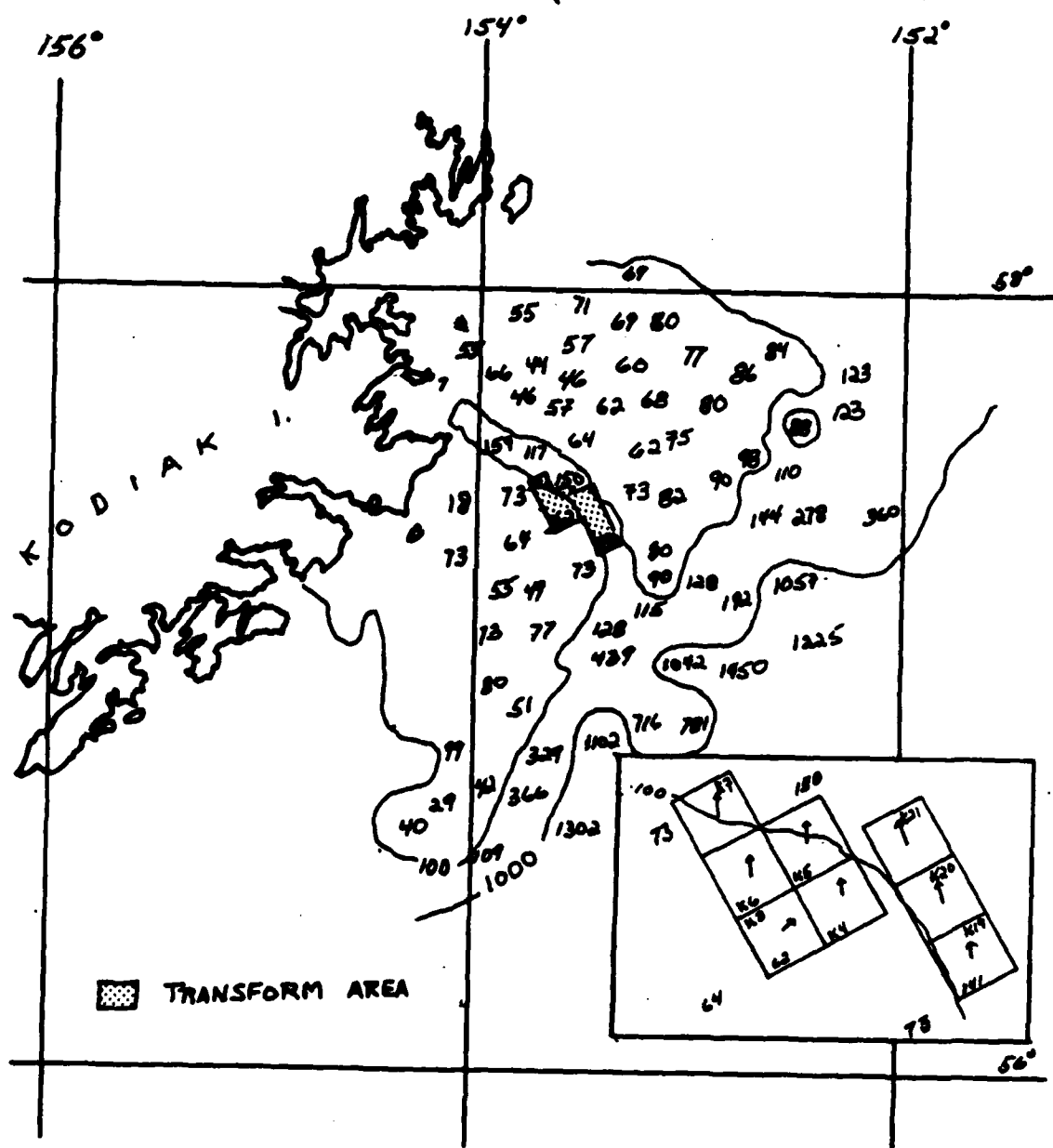


Figure 4.18. Water depths in Area VIII, (depths in meters, scale 1:250,000).

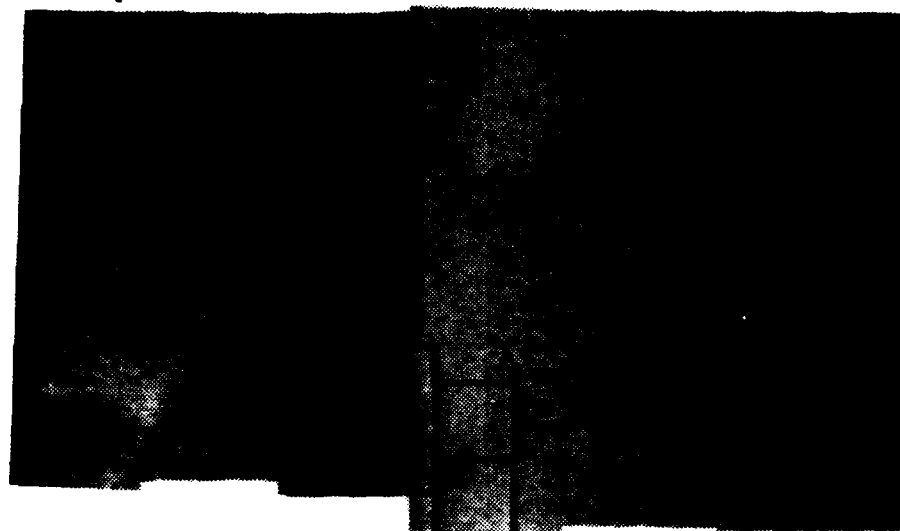


Figure 4.19. Imagery from revolution 811 covering Area VIII, with transform locations.

Figure 4.18 shows the wavelengths and directions in relation to charted depths for the area. Transform areas K3 and K4 have somewhat shorter wavelengths than the other areas and there is a general increase in wavelengths moving from left to right (from shallow water to deep) across the transform areas. However, the wavelength in K19 is equivalent to that in K3 and K4, and the water depth in K19 is significantly deeper, according to the charted depths. The data in the diagram and Table 4.7 indicate a subsequent increase in depth moving from left to right.

Depth ranges and effective median depths were predicted for four transform areas, K6, K4, K20 and K19. The depth range in area K7 is 70 to 140 m with an effective median depth of 105 m. These values were used to predict a depth range of 50 to 96 m and an effective median depth of 73 m in area K6. The actual depth range and effective median depth in K6 are 70 to 100 m and 85 m (14-percent error), respectively.

The depth range and effective median depth for K4 were predicted using the depth range in K5, 75 to 145 m with an effective median depth of 110 m. The predicted depth range in K4 is 46 to 84 m with an effective median depth of 66 m compared to the actual range of 70 to 100 m with an actual effective median depth of 85 m (22-percent error).

The depth range in area K21 is 100 to 160 m and the effective median depth is 130 m, which were used to

calculate the predicted depth range and the effective median depth in area K20. The predicted depth range for K20 of 58 to 88 m with an effective median depth of 73 m, compared to an actual 100 to 140 m range with an effective median depth of 125 m, has a 42-percent error. The charted data from area K20 was also used to calculate a predicted effective median depth and range for area K19. The K19 predicted values are 63 to 90 m with an effective median depth of 77 m and the actual range is 100 to 150 meters with an effective median depth of 125 m, a 38-percent error.

Since the depths are taken from a small-scale navigation chart (scale 1:2,100,000), it is possible that the K19 and K20 transform area wavelengths (shown in deep water) may indicate an uncharted extension of the shoal. Moreover, the change in wave direction between areas K21, K20 and K19 would be more consistent if the 100 m depth curve were extended out into the channel at the locations of K19 and K20.

C. SUMMARY

Analysis of SAR images for eight case study areas in Shelikof Strait revealed many instances where significant bathymetric features were indicated by, 1) internal wave signatures, 2) radar cross-section anomalies, or 3) wave refraction detected from OFT's. Where possible, the mechanisms which caused anomalous patterns to appear in the

SAR imagery were described, and error budgets were calculated for the depths predicted from wave refraction. While there was one negative example, the analysis produced many positive examples.

1. Internal Waves

Three cases of internal wave signatures were observed in the SAR imagery of Shelikof Strait, and each signature was distinct from the other two. The internal wave propagating towards Augustine Island in Area I (identified by its SAR signature, a single wavetrain), is possibly generated by interaction of the internal tide with the shelf edge.

A second internal wave signature appeared in the SAR imagery of Area II; a set of curved wave packets appearing to propagate outward from a single point source. The observed location of this internal wave signature is consistent with generation by interaction of the internal tide (during peak flood stage) with the seamount in the northeast entrance to Shelikof Strait.

The third internal wave signature appeared in the SAR imagery for Area VII at the edge of a dramatic change in the backscatter intensity that may result from the presence of a fresh-water runoff lens. Density stratification occurs where there is a cold, fresh-water layer on the surface and the warmer, more saline ambient water lies on the bottom. When this occurs over a shelf with a steep slope into deeper

water, the self break tends to inhibit mixing of the layers, enforcing the stratification. Thus, interaction between water flow and the shelf break will tend to generate internal waves which appear near the edge of the fresh-water lens (Fig. 34 in Fu and Holt, 1982). Hence, the appearance of internal waves near the edge of a fresh-water lens would indicate a steep shelf break.

2. Brightness Anomalies

There were a number of cases where brightness anomalies in the SAR imagery could be related to either a shoaling bottom or a bathymetric feature. In Area II, a large anomaly appeared which, together with the internal wave signature discussed above, helped locate the large seamount near the northeast entrance of Shelikof Strait. In this case, the anomaly was backscatter return from surface waters directly above the seamount.

The brightness anomaly in Area IV corresponds to an area shown on the bathymetric map as having rocks awash. Thus, the increased brightness was likely due to modulation of the surface water's radar cross-section as well as to possible reflections from the rocks.

In Area V, elongated brightness anomalies corresponding to a shoal area on the bathymetric map appeared in both SAR images of the area, and in Area VI there were several anomalies corresponding to a rough, irregular bottom topography. The increased backscatter

intensity from these areas is likely due to interaction between water flow and the rough bottom, modulating the Bragg waves and radar cross-section on the sea surface.

Anomalies were expected to appear near Augustine Island (where rocks are known to break the surface), but did not (see analysis of Area I). There were also some cases where anomalies appeared, but the processes which produced them are not understood.

In Area I, there are a number of rocky areas and rough bathymetry to the southeast of Augustine Island which should have modulated the surface radar cross-section and created brightness anomalies in the SAR imagery. However, no anomalies corresponding to these features appeared, possibly because the tide waters were too high for interactions between water flow and the bottom to modulate the surface radar cross-section. It is unclear, given the lack of information on prevailing oceanographic conditions, why this feature failed to produce an anomaly in the SAR imagery. This example clearly emphasizes that the absence of a brightness anomaly, or any other indicator of a shoal, in SAR imagery, can in no circumstances be interpreted as implying that an area is safe for navigation.

Scalloped, bright lines appeared in the imagery for Area III, which seemed to parallel the escarpment shown in the bathymetry. However, the lines are 2-10 km from the escarpment and the general water flow runs parallel to the

bathymetry. Thus, while the relationship between the anomalies and the escarpment is not clear, the information can still be useful in locating bathymetric features.

A similar type of bright line appears in the imagery for Area VII, situated roughly above a shelf break. The upper portion of the line appears to be the boundary of a fresh-water lens depicting the density stratification situation described previously. However, part of the lens' boundary crosses a canyon shown on the bathymetric map. The lower portion of the line does not appear to be associated with the fresh-water lens, but it is situated directly over the shelf break. Again, the mechanisms which produced the anomalous radar cross-section are not certain; however, the anomaly does appear to be related to the bathymetry and an interpretation of its presence can be useful.

3. OFT Analyses

Thirty areas in this study had a dominant wave spectra measurable by OFT (Table 4.8). Depth ranges and effective median depths were predicted for fourteen of the thirty areas.

The predicted depth ranges and predicted effective median depths were calculated for a given transform pair using the OFT-measured wavelengths for each transform area and the depths shown in bathymetric maps of the area. The depth range and effective median depth for each transform area were determined by inspection of the bathymetry. In

Table 4.8 Optical Fourier Transform Data

Transform Pair	Area	Wavelength (meters)	Change in Wavelength (meters)	Direction	Change in Direction
B15 to B14	I	1,825 378	1,447	18 348	30
B15 to B16	I	1,825 935	890	18 20	2
A23 to A22	II	1,160 845	315	175 180	5
A26 to A22	II	856 845	11	170 180	10
A8 to A4	III	2,362 1,150	1,212	189 181	8
A5 to A4	III	1,342 1,150	192	175 181	6
A27 to A30	IV	970 836	125	179 182	3
A30 to A31	IV	836 784	52	173 177	4
D17 to D16	V	902 588	314	358 346	12
G1 to G2	V	796 699	97	284 292	8
F2 to F1	V	1,229 722	507	19 4	15
F2 to F4	V	1,229 1,106	123	19 9	10
C9 to C8	VI	543 533	10	323 325	2
C6 to C7	VI	838 658	180	326 326	0
K7 to K6	VIII	1,271 1,075	196	179 182	3
K5 to K4	VIII	1,165 923	242	181 179	2
K21 to K20	VIII	1,388 1,068	320	164 167	3
K20 to K19	VIII	1,068 866	202	167 176	9

the transform area having the longer wavelength (as determined from the OFT) the minimum and maximum depths were used in equation 4.2 to calculate estimates of the wave period. These wave periods were then used to estimate minimum, maximum and effective median depths associated with the other transform area.

Transform areas B15/B14 and B15/B16 were excluded from the analysis because the large change in wavelength over such a short distance makes it improbable the OFT-measured spectra are from the same wavetrain. Also, transform areas D17/D16 were excluded because the areas' wavelengths were opposite from the tendency expected for onshore propagation of a wave group. In operational practice, this pair would be flagged as a probable "artifact" and set aside pending independent corroboration from subsequent SAR images.

The predicted effective median depth was compared to the actual effective median range as determined from a bathymetric map and the error associated with the prediction was calculated by

$$\text{Error} = \left(\frac{\text{actual eff. median depth} - \text{predicted median depth}}{\text{actual effective median depth}} \right) \times 100.$$

The results of the predictions are given in Table 4.9. In general, the quantitative results are respectable. Ten of

Table 4.9 Optical Fourier Transform Prediction Accuracy

Transform Pair	Actual Depth Range (m)	Actual Effective Median Depth (m)	Predicted Shoaling Ratio	Predicted Effective Median Depth (m)	Predicted Depth Range (m)	Predicted Median Depth Error (%)
B15 to B14	--	--	--	--	--	--
B15 to B16	--	--	--	--	--	--
A23 to A22	125-160	145				
A26 to A22	110-160	135	0.53	70	62-76	48
A5 to A4	100-160	150				
A27 to A30	110-160	135	0.97	144	94-148	7
A30 to A31	170-200	190				
D17 to D16	50-200	150	0.73	130	117-135	13
G1 to G2	150-185	170				
F2 to F1	50-190	135	0.74	113	102-120	16
F2 to F4	50-190	135				
C9 to C8	30-175	102	0.88	113	44-151	11
C6 to C7	--	--	--	--	--	--
K7 to K6	25-65	40				
K5 to K4	30-75	35	1.00	31	19-48	11
K21 to K20	50-125	95				
K19	20-45	32	0.35	31	17-40	3
	50-125	95				
	65-130	97	0.81	76	40-99	22
	120-200	170				
	45-110	80	0.96	150	108-153	88
	140-195	170				
	45-135	90	0.62	85	75-99	6
	70-140	105				
	70-100	85	0.72	73	50-96	14
	75-145	110				
	70-100	85	0.63	66	46-84	22
	100-160	130				
	100-150	125	0.59	73	58-88	42
	100-150	125				
	100-150	125	0.66	77	63-90	38

the fourteen predicted effective median depths had an error less than 30-percent, with a mean error of 24-percent.

Predicted depth ranges, on the other hand, are consistently less than the actual depth ranges (Table 4.9). This occurs because the wave refraction estimated using OFT's selects a result consistent with the effective median depth for the area covered by each transform; the relatively small areas typically associated with shoalest and deepest depths in a pair of transform areas are simply not well represented by refraction of the dominant wave. Overall, the ratios of actual to predicted shoalest depths average 1.16 and range from 0.42 to 1.77, and for deepest depths the ratios average 1.38 and range from 0.72 to 2.28. In cases where a reasonable prediction of median depth was obtained (30-percent or better), the ratios of actual to predicted shoalest depths averaged 1.07 and ranged from 0.42 to 1.63, and the ratios for deepest depths averaged 1.29 and ranged from 1.04 to 1.58.

V. DISCUSSIONS AND CONCLUSIONS

A. DISCUSSION

This study has explored the feasibility of using SAR imagery to locate hazards to navigation, thus enabling charting organizations to better utilize their limited resources. Analyses of anomalous patterns in SAR imagery of Shelikof Strait, Alaska, and wave refraction analysis using OFT-measured wave spectra were performed.

Synthetic aperture radar imagery collections are generally not restricted by weather, cloud cover or hours of sunlight. Therefore, SAR sensors have an advantage over passive sensors, such as LANDSAT, for providing a quick-response capability to military charting organizations. As a military planning tool SAR can provide information on the safety of navigating through infrequently used waters, hostile areas, or waters which experience heavy cloud cover for much of the year, such as in South America. An analyst could provide information on these types of areas in a matter of days at a cost of hundreds of dollars, where it might take an advance survey party several weeks and tens of thousands of dollars to obtain the same information.

Non-military charting organizations would also realize benefits by utilizing SAR imagery as a presurvey or planning tool. Where an organization has several areas to survey,

and only enough funds to survey some of them, SAR images would reveal those areas with the most critical hazards to navigation, and thus requiring immediate attention. Again, SAR images would provide this information at a potential savings of tens of thousands of dollars.

Anomalies occur in SAR imagery of ocean surfaces due to oceanographic and atmospheric processes modulating the sea surface radar cross-section. This study examined SAR imagery of Shelikof Strait, Alaska in an attempt to relate visual anomalies to bathymetric features and to locate shoal areas from OFT-measured wave spectra using wave refraction.

A large seamount, a change in the ocean bottom slope and a shelf break were located using the signature in the surface radar cross-section left by the interaction between internal waves and these features. Anomalous patches in the imagery were related to shoal areas, rocks awash, seamounts and freshwater lenses. Bright lines in the imagery were observed over or near escarpments and shelf breaks.

In addition, linear wave theory was used to estimate shoaling ratios and depth ranges from OFT-measured wave spectra and wave refraction. The OFT-measured wavelengths and wave directions were obtained for locations in the study area most likely to experience measurable wave refraction. Predicted depths and shoaling ratios were compared to actual values determined from bathymetric maps, and an error calculated for the prediction. While the quality of the

results varied, in most cases the OFT-measured spectra qualitatively indicated the areas with the shoaler waters.

This study also pointed out some risks involved with using the image analysis and the wave refraction analysis to locate hazards to navigation. In the image analysis portion of the study there were some areas where navigation hazards were known to exist, but which did not appear in the imagery (e.g., the rocky areas around Augustine Island in Area I). In the wave refraction analysis, there was one case (transform areas D17 and D16 in Area V) where the difference in wavelengths suggested the opposite sense of shoaling. However, this case can be flagged as a probable artifact without prior knowledge of the actual bathymetry on the grounds that it is unreasonable to expect wavelengths to increase during onshore propagation; in practice this OFT case would be flagged as an artifact pending confirmation by subsequent SAR images. Transform areas B15/B16 and B14/B15 were also rejected on the apriori basis that it is unlikely a wavetrain could experience wavelength shortening of over 1 km over a distance of 5 km, without breaking.

Caution and prudence must be exercised when interpreting the results of SAR analysis for detecting hazards to navigation. If an anomaly appears in the imagery, a bathymetric feature is likely to exist in the area, but the absence of a signature does not necessarily imply that an area is hazard-free. In SAR OFT wave refraction analysis,

observed changes in wavelength are not always correct indicators of shoaling; an analyst must also consider the magnitude of the change and other circumstances to ascertain whether the two spectra are likely to represent refraction of a single wavetrain.

Independent knowledge of environmental conditions, such as tides, tidal currents and wind patterns is also necessary for correct interpretations of SAR images. Proper ground truth information, such as tidal heights, actual times for the tides, weather conditions and both surface and subsurface current data, would have significantly enhanced this study. The lack of concurrent oceanographic and meteorological data has imposed the need for speculative interpretations of many of the phenomena observed in the study. Future research projects and operational applications of this technique should include provisions for concurrent acquisition of these data whenever possible.

B. CONCLUSIONS

The results of this study show that SAR images contain potentially useful information about shoals and other bathymetric features. An experienced, trained analyst could use SAR imagery to derive valuable presurvey information for planning hydrographic surveys. He could identify potential hazards to navigation, determine the general shape of the bathymetry using SAR signatures, and identify areas and

approximate depths of shoaling waters using OFT analysis to measure wave refraction. This information could then be used to assign priorities to areas to be surveyed.

An analyst should not, however, expect to assign accurate depths to any areas based on either visual information or OFT analysis alone. Furthermore, while SAR images often indicate navigational hazards, the absence of anomalies does not mean there are no hazards present.

This study also shows that wave refraction can be measured by OFT's well enough to warrant further study, albeit in an area where the refraction can be more easily measured. Most of the areas studied here are sheltered from the Pacific swell, and the waves illuminating the bathymetric features were locally wind generated waves of presumably smaller amplitude and wavelength. Shelikof Strait is, therefore, perhaps not the ideal test area for exploring the application of SAR-measured wave refraction (using OFT's) to detect shoals; a study of Pacific atolls, which are illuminated by relatively large amplitude swell generated by storm winds with virtually unlimited fetch is likely to be more conclusive. From this standpoint it would have been better to have evaluated SAR imagery from such reasonably well-charted Pacific islands as Guam, Yap, Saipan, Iwo Jima, Okinawa, and various islands and reef/shoals in the Hawaiian Archipelago. These shoals are well illuminated with Pacific swell, and many areas are

reasonably well surveyed. In addition, such a study would have been valuable in highlighting possible uncharted shoals in subareas which have not been recently surveyed.

Despite the difficulties in analyzing a sheltered area such as Shelikof Strait, there is clearly valuable information to be gained through SAR imagery analysis. A trained analyst who is experienced in interpreting oceanographic and meteorological phenomena, and who also understands the radar imagery, could develop a presurvey bathymetric feature analysis which could lead to significant cost savings in survey implementation. In addition, this analysis would enhance the safety of survey operations by alerting shipboard personnel to locations of possible navigational hazards.

C. RECOMMENDATIONS

The results of this study lead to several recommendations for further work in SAR imagery analysis and for utilizing that analysis. Additional research is necessary to better determine the accuracy of depth inferences from wave refraction measured by OFT's of SAR imagery. This research should be in an area open to the ocean, where the OFT can track wavetrains as they change from large amplitude, deep-water swell through transition waves to shallow-water waves. Also, the transform areas should overlap, such as transform areas A30 and A31 in Area

IV, rather than having discrete transform areas, as was the case throughout most of this study. This would provide a better tracking capability and possibly provide information on exactly where different wavetrains begin to mix such that there is no dominant wave spectra.

A second recommendation is that further work be done to evaluate systematic procedures for subjective and semi-quantitative interpretation of brightness anomalies and internal wave signatures. These methods should also incorporate information on local oceanographic, meteorological, and hydrological (i.e., river runoff) conditions to allow less ambiguous interpretations of certain features, and to allow a better discrimination of possible wind stress anomalies than was possible in this study.

The third recommendation is that existing SAR data be utilized in an interpretive mode as part of the operational presurvey planning process. Image analysts with experience in both oceanographic and radar phenomena can extract valuable information from SAR imagery, and both interpretive methods and procedures for using such information in planning surveys can be best developed in an operational environment. Once surveying and charting organizations make a commitment to utilizing SAR imagery, the methods and procedures developed should lead to significant improvement in efficiency and cost-effectiveness of survey operations.

LIST OF REFERENCES

- Alpers, W.R., D.B. Ross and C.L. Rufenach, 1981. On the detectability of ocean surface waves by real and synthetic aperture radar, J. Geophys. Res., 86, pp6481-6498.
- Alpers, W., 1983. Imaging ocean surface waves by synthetic aperture radar - a review, pp107-119 in: Allan, T.D. (ed.), Satellite Microwave Remote Sensing, Chichester, Ellis Horvath Limited.
- Alpers, W. and S. Ettore, 1983. Scylla and Charybdis observed from space, J. Geophys. Res., 88, pp1800-1808.
- Apel, J.R., H.M. Byrne, J.R. Proni and R.L. Charnell, 1975. Observations of oceanic internal and surface waves from the Earth Resources Technology Satellite, J. Geophys. Res., 80, pp865-881.
- Arthur, R.S., 1965. On the calculation of vertical motion in eastern boundary currents from determinations of horizontal motions, J. Geophys. Res., 70, pp2799-2803.
- Brown, W.E. Jr., C.Elachi and T.W. Thompson, 1976. Radar imaging of ocean surface patterns,, J. Geophys. Res., 81, pp2657-2667.
- Coastal Engineering Research Center (CERC), Shore Protection Manual, vl, Department of the Army, US Army Corps of Engineers, 1984.
- Collins, J., 1978. Cost benefits of photobathymetry, paper presented at the Coastal Mapping Symposium, Rockville, MD.
- Evans, D.D. and O.H. Shemdin, 1980. An investigation of the modulation of capillary and short gravity waves in the open ocean, J. Geophys. Res., 85, pp5019-5024.
- Fu, L. and B. Holt, 1982. SEASAT Views Oceans and Sea Ice With Synthetic Aperture Radar, JPL Pub; 81-120, Jet Propulsion Laboratory, Pasadena, CA 200p.
- Goldsteen, G.H., 1982. The navigability of waterways, The Hydrographic Jour., July issue, pp25-45.
- Goodfellow, D., 1982. Sailing uncharted seas, The Hydrographic Jour., October issue, p23.

- Goodman, J.W., 1968. Introduction to Fourier Optics, San Francisco, 287p.
- Hammack, J.C., 1977. Landsat goes to sea, Photogrammetric Engineering and Remote Sensing, 43, pp683-691.
- Hays, J.G., 1980. Ocean current wave interaction study, J. Geophys. Res., 85, pp5025-5031.
- Hughes, B.A. and J.F.R. Gower, 1983. SAR imagery and surface truth comparisons of internal waves in Georgia Strait, British Columbia, Canada, J. Geophys. Res., 88, pp1809-1824.
- Kasischke, E.S., R.A. Shuchman and J.D. Lyden, 1980. Detection of bathymetric features using SEASAT synthetic aperture radar - a feasibility study, Environmental Research Institute of Michigan Report No. 135900-2-F², Ann Arbor, MI.
- Kasischke, E.S., D.R. Lyzenga, R.A. Shuchman, Y.S. Tseng, B.S. Termaat, B.A. Burns and G.A. Meadows, 1982. The use of synthetic aperture radar to detect and chart submerged navigation hazards, Environmental Research Institute of Michigan Report No. 155200-1-F, Ann Arbor, MI.
- Kasischke, E.S., R.A. Shuchman, D.R. Lyzenga and G.A. Meadows, 1983. Detection of bottom features on SEASAT synthetic aperture radar imagery, Photogrammetric Engineering and Remote Sensing, 49, pp1341-1353.
- Knauss, J.A. 1978. Introduction to Physical Oceanography, Englewood Cliffs, NJ, Prentice-Hall, 338p.
- LeBlond, P.H. and L.A. Mysak, 1978. Waves in the Ocean, New York, NY, Elsevier Scientific Publishing Co, 602p.
- McLeish, W., D. Ross, R.A. Shuchman, P.G. Teleki, S.V. Hsiao, O.H. Shemdin and W.E. Brown, Jr., 1980. Synthetic aperture radar imaging of ocean waves: comparison with wave measurements, J. Geophys. Res., 85, pp5003-5011.
- Meadows, G.A., R.A. Shuchman, Y.C. Tseng and E.S. Kasischke, 1983. SEASAT synthetic aperture radar observations of wave-current and wave-topographic interactions, J. Geophys. Res., 88, pp4393-4406.
- Mooers, C.N.K., C.N. Flagg, and W.C. Boicourt, 1978. Prograde and retrograde fronts, p43 in: Bowman, M.J. and W.E. Esaias (eds.), Oceanic Fronts in Coastal Processes, New York, Springer-Verlag.

- Muench, R.D., H.O. Mofjeld and R.L. Charnell, 1978. Oceanographic conditions in Lower Cook Inlet: spring and summer 1973, J. Geophys. Res., 83, pp5090-5098.
- Muench, R.D. and J.D. Schumacher, 1980. Physical oceanographic and meteorological conditions in the Northwest Gulf of Alaska, NOAA Technical Memorandum ERL PMEL-22, National Oceanic and Atmospheric Administration, Seattle, WA.
- Mysak, L.A., R.D. Muench and J.D. Schumacher, 1981. Baroclinic instability in a downstream varying channel: Shelikof Strait, Alaska, J. Phys. Ocean. 11, pp950-969.
- Pawka, S.S., S.V. Hsiao, O.H. Shemdin and D.L. Inman, 1980. Comparisons between wave directional spectra from SAR and pressure sensor arrays, J. Geophys. Res., 85, pp4987-4995.
- Phillips, O.M., 1981. The structure of short gravity waves on the ocean surface, pp24-31 in: Beal, R.C., P.S. DeLeonibus and I. Katz (eds.), Spaceborne Synthetic Aperture Radar for Oceanography, Baltimore, MD. Johns Hopkins Univ. Press.
- Plant, W.J., W.C. Keller and J.W. Wright, 1978. Modulation of coherent microwave backscatter by shoaling waves, J. Geophys. Res., 83, pp1347-1352.
- Redfield, A. C., 1980. Introduction to Tides, Woods Hole, MA, Marine Science International, 108p.
- Schaffer, G., 1976. A mesoscale study of coastal upwelling variability off NW Africa, Meteor "Forsch.-Ergebn. A", 17, pp21-72.
- Shuchman, R.A. and E.S. Kasischke, 1979. The detection of oceanic bottom topographic features using SEASAT synthetic aperture radar imagery, paper presented at the thirteenth Int'l Symposium on Remote Sensing of Environment, Ann Arbor, MI.
- Shuchman, R.A. and E.S. Kasischke, 1981. Refraction of coastal ocean waves, pp128-135 in: Beal, R.C., P.S. DeLeonibus and I. Katz (eds.), Spaceborne Synthetic Aperture Radar for Oceanography, Baltimore, MD, Johns Hopkins Univ. Press.

Shuchman, R.A., E.S. Kasischke, A. Klooster and P.L. Jackson, 1979. SEASAT SAR coastal ocean wave analysis: A wave refraction and diffraction study, Environmental Research Institute of Michigan Final Report No. 138600-2-F, Ann Arbor, MI.

Shuchman, R.A., A.L. Maffett and A. Klooster, Jr., 1981. Static and dynamic modeling of a SAR imaged ocean scene, IEEE J. Ocean. Eng., OE-6, pp41-49.-6, pp41-49.

Thompson, R.O.R.Y. and T.J. Golding, 1981. Tidally induced 'upwelling' by the Great Barrier Reef, J. Geophys. Res., 86, pp6517-6521.

Thompson, T.W., D.E. Weissman and F.L. Gonzalez, 1983. L-band radar backscatter dependence upon surface wind stress: A summary of new SEASAT-1 and aircraft observations, J. Geophys. Res., 88, pp1727-1735.

Tomiyasu, K., 1976. Phase and Doppler errors in a spaceborne synthetic aperture radar imaging the ocean surface, IEEE J. Ocean. Eng., OE-1, pp68-71.

Trask, R.P. and M.G. Briscoe, 1983. Detection of Massachusetts Bay internal waves by the synthetic aperture radar (SAR) on SEASAT, J. Geophys. Res., 88, pp1789-1799.

Tucker, M.J., 1983. The effect of a moving sea surface on SAR imagery, pp147-154 in: Allan, T.D. (ed.), Satellite Microwave Remote Sensing, Chichester, Ellis Horwood Limited.

Valenzuela, G.R., D.T. Chen, W.D. Garrett and J.A.C. Kaiser, 1983. NRL remote sensing experiment, EOS, 64, pp618-619.

Vesecky, J.F. and R.H. Stewart, 1982. The observation of ocean surface phenomena using imagery from the SEASAT synthetic aperture radar: An assessment, J. Geophys. Res., 87, pp3397-3430.

Wunsch, C., 1968. On the propagation of internal waves up a slope, Deep Sea Res., 15, pp251-258.

APPENDIX A: OPTICAL FOURIER TRANSFORMS

A. APPLICATION TO WAVE REFRACTION

Experiments by Abbe and Porter (Goodman, 1968), showed that coherent, collimated light passing through an object transparency and then through a lens separates the object pattern into its Fourier components at the transform lens' focal plane (Fig. A.1). A simple illustration of the transform is shown in Figure A.2. If the transparency has a pattern similar to the one in Figure A.2a, then the Fourier components shown in Figure A.2b will appear at the focal plane. The distance from the origin of the axes to the first dot is the k -space wavelength, or wave number, of the fundamental harmonics. It also follows that the distance from the origin to each succeeding dot is representative of the next higher harmonics. If the pattern shown in Figure A.2a is rotated as shown in Figure A.3a, the subsequent transform also rotates as shown in Figure A.3b.

B. GENERATING THE OFT

Optical Fourier Transforms (OFT), were generated using a helium-neon laser mounted on an optical bench (Fig. A.4). The laser beam is expanded using a pinhole device and

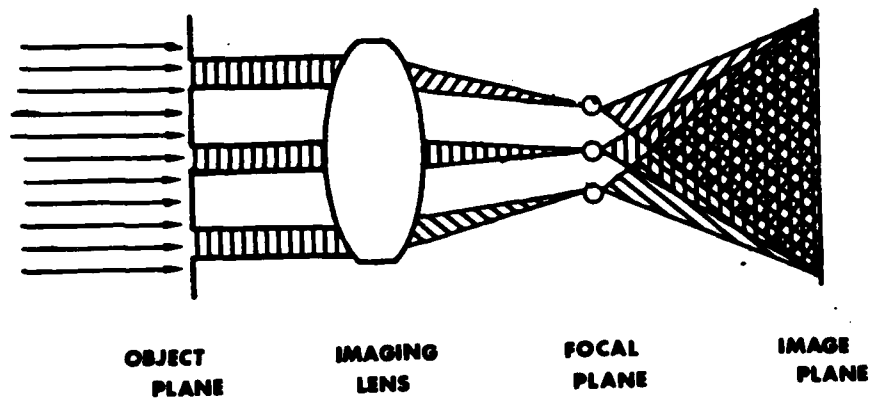


Figure A.1. Optical Fourier Transform.

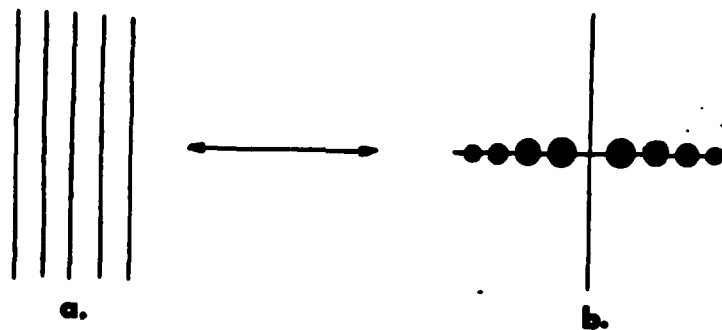


Figure A.2. OFT of evenly-spaced grating.

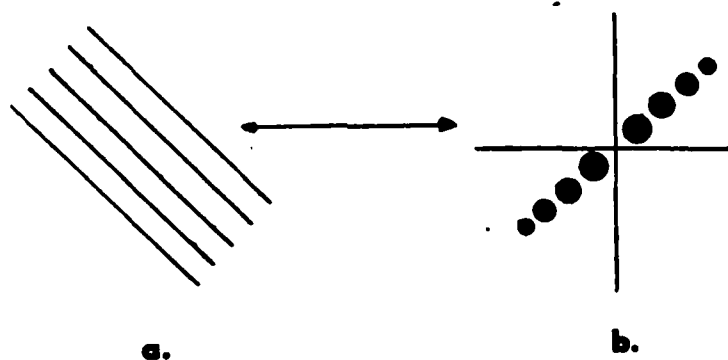


Figure A.3. OFT of evenly-spaced grating after rotation.

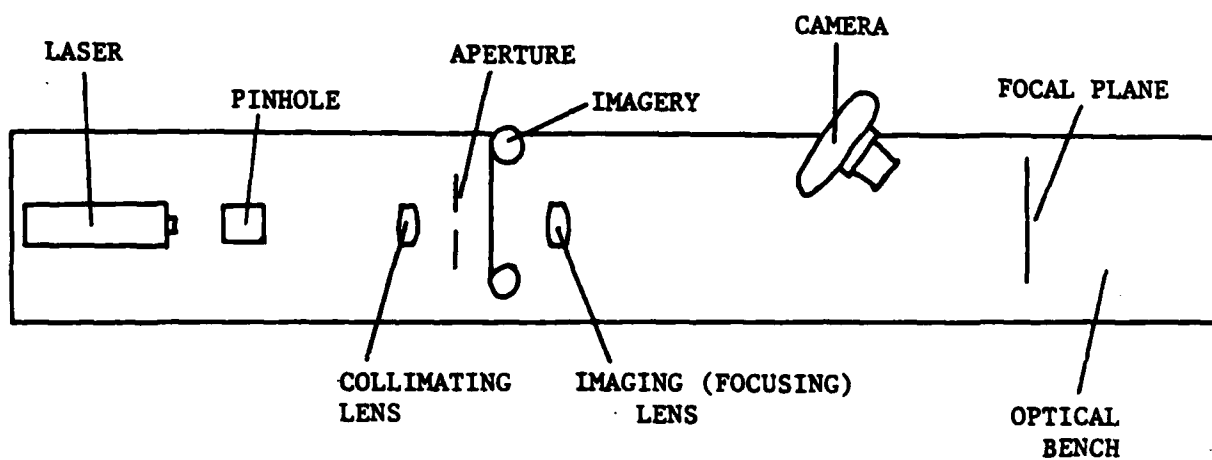


Figure A.4. Optical bench set-up.

collimated using a lens placed so the pinhole is at its focal point.

The distance between the two lenses must allow a roll of film and a plate containing the focusing aperture to pass between them. The transform of an object on a film transparency occurs at the focal plane of the second lens (Fig. A.1). To focus the laser beam on a particular area of the imagery, a metal plate with a 1 cm^2 aperture was inserted between the collimating lens and the film imagery. With the scale of the imagery at 1:500,000 it was possible to determine the dominant wavelength and wave direction for any given 25 km^2 area.

The transforms were displayed on a piece of white cardboard, (with calibration marks), placed in the focal plane and then photographed. A small hole in the cardboard was aligned with the center of the transform to allow the intense light of the center beam, and very long wave components, to pass through; if this was not done, the desired transforms could not be distinguished from background brightness in the photographs.

C. TRANSFORM MEASUREMENTS

The transform wave number components were measured using a zoom transfer scope. Using the geometry of Figure A.5,

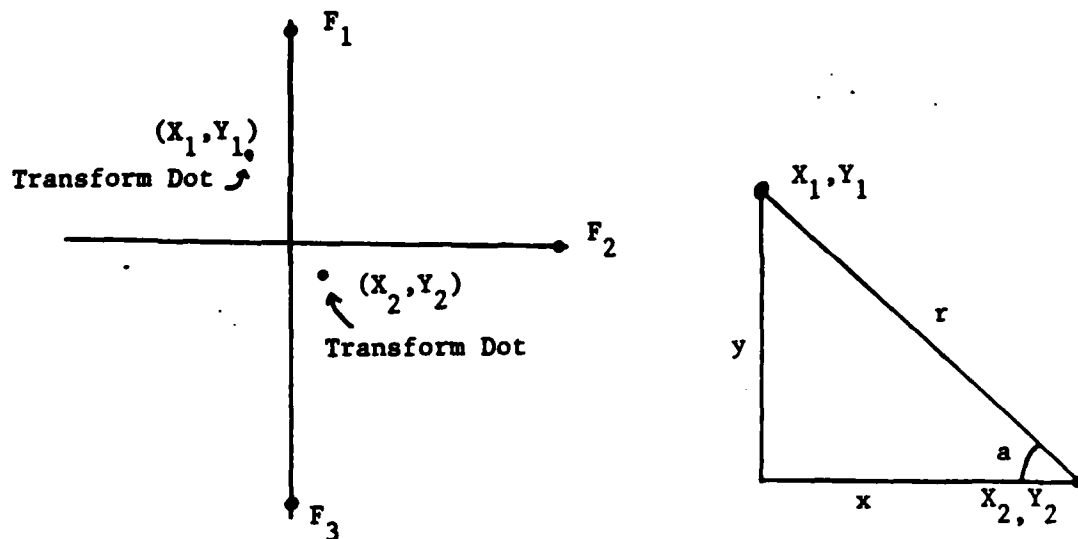
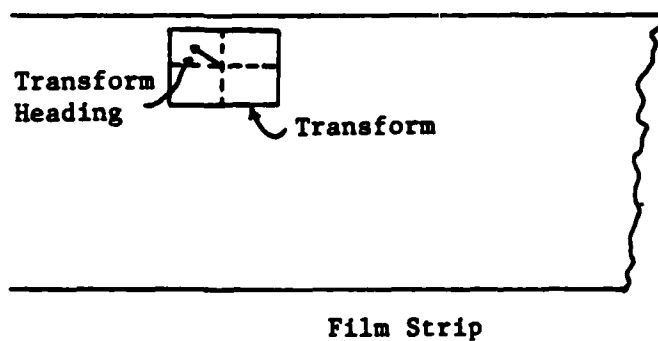


Figure A.5. k-space wavelength.



NOTE: Transform area was always oriented as shown.

Figure A.6. Transform wave heading

$$x = (1/dx)(x_2 - x_1) \text{ and,}$$

$$y = (2/dy)(y_1 - y_2),$$

where dx is the measured image distance between F_2 and the origin, dy is the measured image distance between F_1 and F_3 .

The scaling factors $1/dx$ and $2/dy$ corrected the coordinate measurements relative to a true dx of 1 cm and a true dy of 2 cm. Thus,

$$r = (x^2 + y^2)^{1/2},$$

and the wavenumber in k -space,

$$r' = (1/2)r,$$

and the transform heading,

$$a = \tan^{-1}(y/x).$$

From Figure A.6, the surface wave structure heading,

$$a'' = a \pm a',$$

where a' is the satellite heading and the sign is determined by the quadrant of the transform heading. In determining

a", it was assumed that surface waves were always propagating shoreward into shoaler water, (with the exception of Area II, section IV.B.2, where the surface waves were assumed to be propagating in a southerly direction.

Four optical fibers were attached by one end to a red light source and the other end placed in the cardboard to produce fiducial marks in the transforms. The ends of the fibers were placed such that each dot was one centimeter from the center hole, and such that if two lines were drawn between each pair of opposing dots, the lines would be orthogonal, creating a rectangular coordinate system with the small hole as the origin. The fiducial marks served to correct for geometric distortion caused by the camera's angle relative to the focal plane, and for other systematic distortions as well.

Photographs were taken using a GAF model L-14 35mm camera with extension tubes between the aperture and lens. The extension tubes allowed the transform display to be mapped onto the camera film at a ratio of almost one-to-one. Otherwise, it would have been necessary to enlarge each photograph in order to make measurements, which would have introduced another error source.

Kodak HIE (High Speed Infrared Film 2481) was used in an entirely darkened room to photograph the transform produced by the red-light laser. The aperture and exposure time

varied according to the brightness of the transform. After the photographs were developed, a zoom transfer scope was used to enlarge them slightly for each measurement. Coordinates in an x,y rectangular coordinate system were then measured for each pair of transform component dots.

The distance from the center hole to each fiducial mark was also measured to correct for distortions caused by camera angle, transform lens and the zoom transfer scope. The scaling factor to correct that measurement to a true 1 cm on both x- and y-axes was applied to the measured coordinates of the transform component dots.

Wavenumber measurement errors were on the order of ± 0.1 mm. This error was a function of the repeatability of each measurement, and is therefore, independent of the actual measured distance. For a measured k-space distance of 1 mm, there is a probable error of 10-percent which, from equation A.2, converts to a surface wavelength error of ± 188 m ($L = 1880$ m). For a k-space measurement of 20 mm, there is a probable error of 0.5 percent, which yields a surface wavelength error of ± 0.5 m ($L = 94$ m). Thus, the shorter the measured k-space distance, the greater the percentage of measurement error.

There are other error sources present on the transforms in the form of distortions due to the quality of the lenses and the lack of precision in the focusing aperture that were used to generate the OFT. Therefore, a direct mapping of

wavelength L on the imagery to the transform is not precise. Since the wavelength on the imagery can be expressed as,

$$A.1 \quad L = 2\pi/k,$$

where k is the wavenumber, we may express the wavelength on the transform as,

$$A.2 \quad L = K/(sr),$$

where K is oceanwave image scale factor (m/mm), s is a dimensionless transform coefficient and r is the measured distance of the transform component from the center hole (mm). Note that the coordinate system was changed from rectangular to polar coordinates for ease of computation in determining wave direction. A transform for a grating of known wavelength was generated, and the distance to the fundamental transform component was measured. For $K=1$, the known values of L and r were substituted in equation A.2 to obtain the value of 0.266 for s . However, for the scale of the imagery at 1:500,000, the value of K is assigned as 500.

APPENDIX B: SURVEY HISTORIES

This appendix summarizes dates, scales and line spacing information on hydrographic surveys in the Shelikof Strait study area.

Figure B.1 shows the geographic locations of the bathymetric maps for Iliamna, Mount Katmai and Afognak used in this study.

Figure B.2, in conjunction with Table B1 gives the survey history for the bathymetric map covering the Afognak area. The labelled area in Figure B.2 is cross-referenced with the appropriate survey date, scale and line spacing to determine the quality of the bathymetric map.

In a similar manner Figure B.3 is cross-referenced with Table B.2 and Figure B.4 with Table B.3 to determine the survey quality of the Mount Katmai and Iliamna areas, respectively.

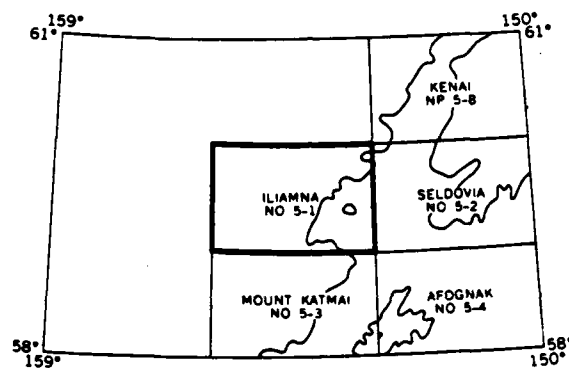


Figure B.1. Index to bathymetric maps.

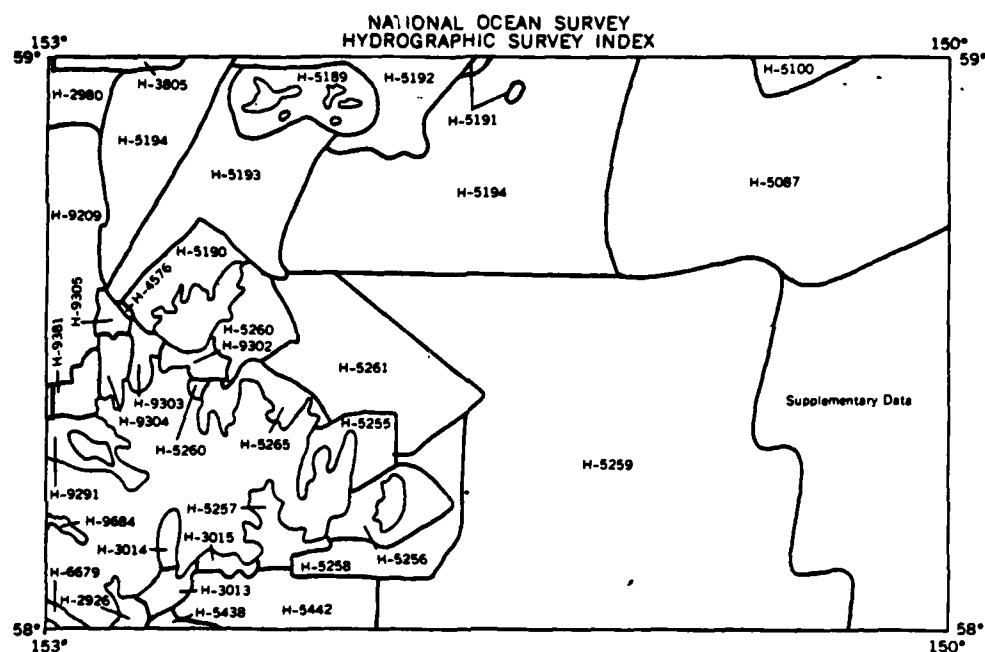


Figure B.2. Survey history for Afognak, NOS No. 5-4.

Table B.1. Survey information for Afognak, NOS No. 5-4.
HYDROGRAPHIC SURVEY INFORMATION

SURVEY NUMBER	SURVEY DATE	SURVEY SCALE	SURVEY LINE SPACING (NAUT. MILES)	SURVEY NUMBER	SURVEY DATE	SURVEY SCALE	SURVEY LINE SPACING (NAUT. MILES)
H-2926	1897	1:20,000	06-41	H-5257	1932	1:20,000	01-50
H-2980	1908	1:200,000	50-40	H-5258	1932	1:40,000	10-30
H-3013	1909	1:20,000	03-50	H-5259	1932	1:160,000	20-27
H-3014	1909	1:20,000	01-12	H-5260	1932	1:20,000	03-20
H-3015	1909	1:20,000	01-27	H-5261	1932	1:40,000	05-60
H-3805	1915	1:120,000	20-29	H-5265	1932	1:20,000	02-40
H-4576	1926	1:20,000	01-38	H-5438	1933	1:20,000	03-35
H-5087	1930	1:160,000	40-22	H-5442	1933	1:40,000	10-40
H-5100	1930	1:80,000	20-10	H-6679	1941	1:10,000	01-10
H-5189	1931	1:20,000	04-15	H-9209	1971	1:40,000	15-50
H-5190	1931	1:20,000	02-20	H-9291	1973	1:20,000	02-20
H-5191	1931	1:40,000	10-40	H-9302	1972	1:10,000	01-22
H-5192	1931	1:40,000	10-45	H-9303	1972	1:10,000	05-14
H-5193	1931	1:40,000	10-45	H-9304	1972-73	1:10,000	02-21
H-5194	1931	1:120,000	10-13	H-9305	1972	1:20,000	01-48
H-5255	1932	1:20,000	10-90	H-9381	1973	1:20,000	07-40
H-5256	1932	1:20,000	01-25	H-9684	1977	1:10,000	02-60

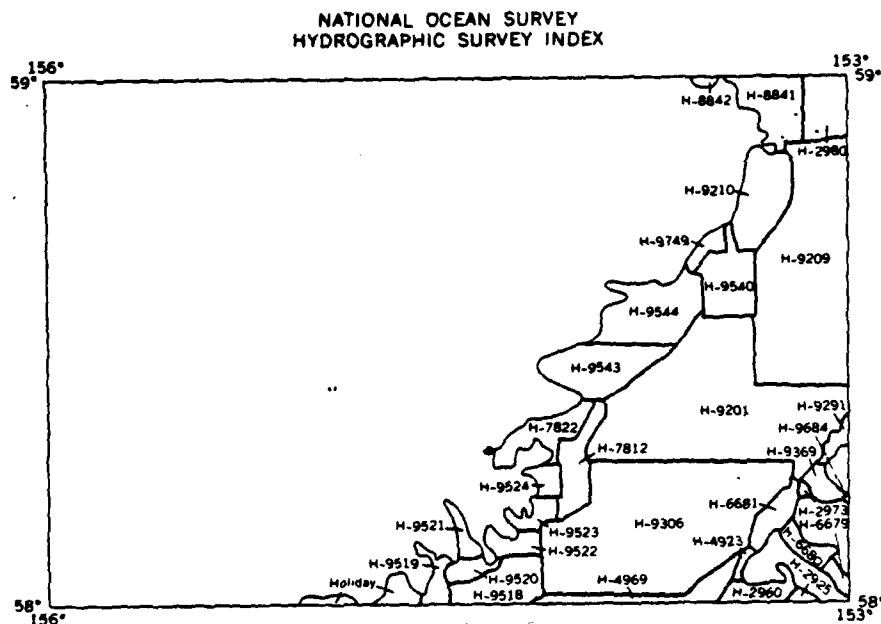


Figure B.3. Survey history for Mt. Katmai,
NOS No.5-3.

Table B.2. Survey information for Mt. Katmai, NOS No. 5-3.
HYDROGRAPHIC SURVEY INFORMATION

SURVEY NUMBER	SURVEY DATE	SURVEY SCALE	SURVEY LINE SPACING (NAUT. MILES)
H-2925	1908	1:20,000	02-26
H-2960	1908	1:20,000	05-40
H-2973	1908	1:20,000	03-30
H-2980	1908	1:200,000	50-40
H-4923	1929	1:20,000	10-30
H-4969	1929	1:100,000	20-40
H-4679	1941	1:10,000	01-10
H-4680	1941	1:10,000	02-50
H-4681	1941	1:20,000	05-22
H-7812	1949	1:40,000	10-30
H-7822	1949	1:20,000	03-17
H-8841	1965	1:20,000	03-50
H-8842	1965-66	1:20,000	03-07
H-9201	1971	1:40,000	20-50
H-9209	1971	1:40,000	15-50
H-9210	1971	1:20,000	02-20
H-9291	1973	1:20,000	02-20
H-9306	1975	1:40,000	20-50
H-9369	1973	1:20,000	04-20
H-9518	1975	1:20,000	05-43
H-9519	1975	1:10,000	02-10
H-9520	1975	1:10,000	02-13
H-9521	1975	1:10,000	05-40
H-9522	1975	1:10,000	12-53
H-9523	1975-77	1:10,000	03-43
H-9524	1975	1:10,000	02-40
H-9540	1975	1:20,000	05-50
H-9543	1975	1:20,000	05-42
H-9544	1975	1:20,000	05-25
H-9684	1977	1:10,000	02-06
H-9749	1977	1:20,000	05-06

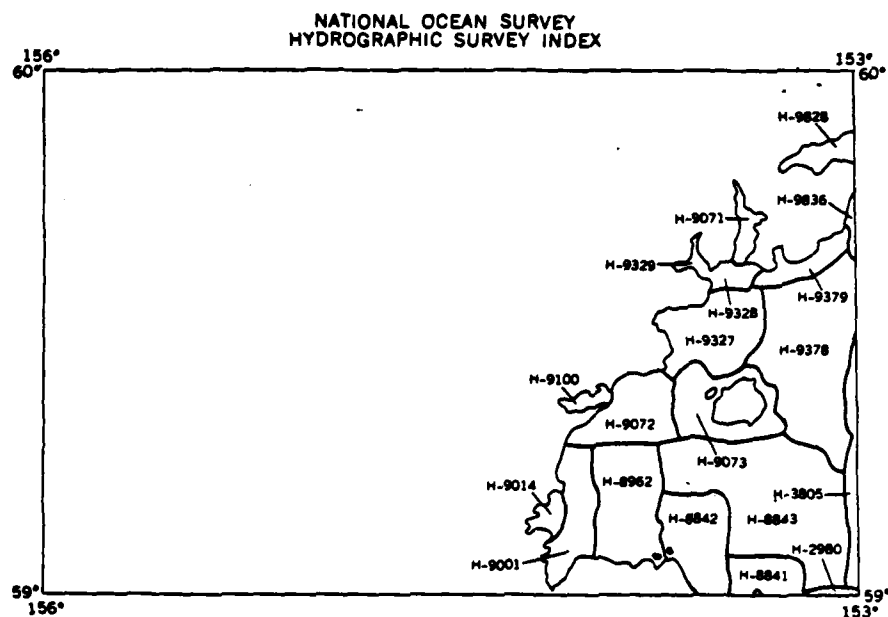


Figure B.4. Survey history for Iliamna, NOS No. 5-1.

Table B.3. Survey information for Iliamna, NOS No. 5-1.

HYDROGRAPHIC SURVEY INFORMATION			
SURVEY NUMBER	SURVEY DATE	SURVEY SCALE	SURVEY LINE SPACING (NAUT. MILES)
H-2980	1908	1:200,000	50-4.0
H-3805	1915	1:120,000	20-2.9
H-8841	1965	1:20,000	03-50
H-8842	1965-66	1:20,000	03-07
H-8843	1968	1:40,000	03-50
H-8962	1967	1:20,000	02-10
H-9001	1968-70	1:20,000	04-06
H-9014	1968	1:10,000	02-05
H-9071	1969	1:10,000	02-08
H-9072	1969-74	1:20,000	06-08
H-9073	1969-74	1:20,000	08-12
H-9100	1968-71	1:10,000	03-15
H-9327	1972	1:20,000	06-10
H-9328	1972-73	1:10,000	03-06
H-9329	1972-73	1:10,000	02-04
H-9378	1973	1:40,000	10-20
H-9379	1973	1:20,000	04-10
H-9828	1979	1:20,000	01-10
H-9836	1979	1:20,000	02-30

INITIAL DISTRIBUTION LIST

	No. Copies
1. Defense Technical Information Center Cameron Station Alexandria, VA 22304-6145	2
2. Library, Code 0142 Naval Postgraduate School Monterey, CA 93943-5100	2
3. Chairman (Code 68Mr) Department of Oceanography Naval Postgraduate School Monterey, CA 93943-5100	1
4. Chairman (Code 63Rd) Department of Meteorology Naval Postgraduate School Monterey, CA 93943-5100	1
5. Dr. James L. Mueller (Code 68My) Department of Oceanography Naval Postgraduate School Monterey, CA 93943-5100	3
6. Ronald L. Dickerman 2902 N. Adams St. Dale City, VA 22193	3
7. Director Naval Oceanography Division Naval Observatory 34th and Massachusetts Avenue, NW Washington, DC 20390	1
8. Commander Naval Oceanography Command NSTL Station Bay St. Louis, MS 39522	1
9. Commanding Officer Naval Oceanographic Office NSTL Station Bay St. Louis, MS 39522	1

- | | | |
|-----|---|---|
| 10. | Commanding Officer
Fleet Numerical Oceanography Center
Monterey, CA 93943 | 1 |
| 11. | Commanding Officer
Naval Ocean Research and Development Activity
NSTL Station
Bay St. Louis, MS 39522 | 1 |
| 12. | Commanding Officer
Naval Environmental Prediction Research Facility
Monterey, CA 93943 | 1 |
| 13. | Chairman, Oceanography Department
U.S. Naval Academy
Annapolis, MD 21402 | 1 |
| 14. | Chief of Naval Research
800 N. Quincy Street
Arlington, VA 22217 | 1 |
| 15. | Office of Naval Research (Code 420)
800 N. Quincy Street
Arlington, VA 22217 | 1 |
| 16. | Scientific Liason Office
Office of Naval Research
Scripps Institution of Oceanography
La Jolla, CA 92037 | 1 |
| 17. | Library
Scripps Institution of Oceanography
P.O. Box 2367
La Jolla, CA 92037 | 1 |
| 18. | Library
Department of Oceanography
University of Washington
Seattle, WA 98105 | 1 |
| 19. | Library
CICESE
P.O. Box 4803
San Ysidro, CA 92073 | 1 |

- | | | |
|-----|---|---|
| 20. | Library
School of Oceanography
Oregon State University
Corvallis, OR 97331 | 1 |
| 21. | Commander
Oceanographic Systems Pacific
Box 1390
Pearl Harbor, HI 96860 | 1 |
| 22. | Director
Defense Mapping Agency
Code PPH
Bldg 56, U.S. Naval Observatory
Washington, DC 20305 | 1 |
| 23. | Director
DMA Hydrographic/Topographic Center
Code HO
Washington, DC 20315 | 1 |
| 24. | Commander and Director
ATTN: D. SKALA, TD-SB
US Army Engineer Topographic Laboratories
Fort Belvoir, VA 22060-5546 | 1 |
| 25. | Bill Cannell
DMA HQ, STA
Suite 810
8301 Greensboro Dr.
McLean, VA 22102 | 1 |
| 26. | Roger Parsons
1705 MacGregory St.
Virginia Beach, VA 23464 | 1 |
| 27. | Robin Muench
Scientific Associates, Inc.
13400B Northrup Way, Suite 36
Bellevue, WA 98005 | 1 |
| 28. | Richard T. Joy
4520 Middleton La.
Bethesda, MD 20814 | 1 |

END

FILMED

12-85

DTIC